Smoothed Phase-Coded FMCW
Waveform Properties and Transceiver Architecture

Kumbul, Utku; Petrov, Nikita; Yarovoy, Alexander; Vaucher, Cicero S.

DOI
10.1109/TAES.2022.3206173

Publication date
2022

Document Version
Final published version

Published in
IEEE Transactions on Aerospace and Electronic Systems

Smoothed Phase-Coded FMCW: Waveform Properties and Transceiver Architecture

UTKU KUMBUL, Graduate Student Member, IEEE
Delft University of Technology, CD, Delft, The Netherlands

NIKITA PETROV
CICERO S. VAUCHER, Senior Member, IEEE
NXP Semiconductors, N.V., Eindhoven, The Netherlands
Delft University of Technology, CD, Delft, The Netherlands

ALEXANDER YAROVOY, Fellow, IEEE
Delft University of Technology, CD, Delft, The Netherlands

Smoothed phase-coded frequency modulated continuous waveform (SPC-FMCW), which is aimed to improve the coexistence of multiple radars operating within the same frequency bandwidth, is studied, and the receiving strategy with a low analog-to-digital converter sampling requirement is investigated. The Gaussian filter is applied to obtain smooth waveform phase transitions, and then, quadratic phase lag compensation is performed before waveform transmission to enhance decoding. The proposed waveform is examined in different domains, and its waveform properties are analyzed theoretically and demonstrated experimentally. Both simulation and experimental results show that the introduced waveform with the investigated processing steps helps combine all advantages of the FMCW waveform, including hardware simplicity and small operational bandwidth of the receiver, with the advantages of phase coding.

Manuscript received 23 March 2022; revised 3 July 2022; accepted 31 August 2022. Date of publication 12 September 2022; date of current version 12 April 2023.

DOI. No. 10.1109/TAES.2022.3206173

Refereeing of this contribution was handled by R.S. Adve.

This work was supported in part by the TU Delft Industry Partnership Program (TIPP), NXP Semiconductors N.V. and Holland High Tech Systems and Materials through the project Coded Radar for Interference Suppression in Super-Dense Environments (CRUISE) under Grant TKI-HTSM/18.0136.

Authors' addresses: Utku Kumbul and Alexander Yarovoy are with the Microwave Sensing, Systems and Signals (MS3) Group, Faculty of Electrical Engineering, Mathematics and Computer Science, Delft University of Technology, 2628 CD Delft, The Netherlands, E-mail: (u.kumbul@tudelft.nl; a.yarovoy@tudelft.nl); Nikita Petrov and Cicero S. Vaucher are with NXP Semiconductors, N.V., 5656 AG Eindhoven, The Netherlands, and also with the Delft University of Technology, Delft, The Netherlands, E-mail: (n.petrov@tudelft.nl; cicero.vaucher@nxp.com). *(Corresponding author: Utku Kumbul).*

I. INTRODUCTION

Radars provide detection, tracking, and classification of targets under various weather conditions. As a consequence, radars are utilized in many areas, such as surveillance, meteorology, defense, and automotive systems. The dramatic increase in the number of radar sensors used for different applications has raised concerns about spectral congestion and the coexistence of radar sensors [1], [2], [3], [4]. The mutual interference between multiple radar sensors downgrades the sensing performance of radar and needs to be mitigated [5], [6], [7], [8]. Moreover, the radar systems used in civil applications (e.g., automotive radar and indoor monitoring) generally have limited processing power, preventing them from using computationally heavy techniques. In order to cope with these issues, designing a robust waveform with a low sampling requirement and improving the independent operation of multiple radars within the same frequency bandwidth is of interest.

Linear frequency modulated continuous waveform (FMCW) has been widely used in civil radar applications [9]. In the FMCW radar, the received signal is mixed with the complex conjugate of the transmitted signal for the stretch processing (also known as dechirping or deramping), which allows small analogue bandwidth of the receiver analogue-to-digital converter (ADC) and a simple hardware structure [10]. Moreover, the FMCW radars can achieve good sensing performance with high resolution. However, the discrimination of FMCW between multiple radars is limited, and the FMCW radars suffer from radar-to-radar interference [11], [12], [13]. For the purpose of unique waveform recognition, waveform coding has been widely used in radars [14]. In particular, phase-modulated continuous waveform (PMCW) provides high mutual orthogonality and, thus, improves the radar's robustness against interference [15], [16], [17]. However, such coding spreads the waveform spectrum over a wide bandwidth and requires a dramatic increase in the receiver's analogue bandwidth.

Lately, phase-coded frequency-modulated continuous waveform (PC-FMCW) has attracted much attention due to taking advantage of both FMCW and PMCW [18], [19], [20]. Applying coding to FMCW improves the waveform diversity and ensures the discrimination of self-transmitted signals from the waveforms transmitted by other radars [21]. Furthermore, PC-FMCW enables joint sensing and communication [22], [23], [24]. In [18], matched filtering is used as a receiver strategy to process PC-FMCW. For the matched filtering operation, the received signal is convolved with the complex conjugate of the transmitted signal. The conventional matched filtering operation in the digital domain demands the acquisition of the received signal with total bandwidth. Hence, this processing approach could not reduce the analogue receive bandwidth, and the key disadvantage of PMCW has been transferred to PC-FMCW. To decrease the waveform sampling requirement in the

receiver, the dechirping-based receiver structures have been studied [20], [21], [22]. In particular, compensated stretch processing has been suggested in [20], where a filter bank has been applied to the sampled data after dechirping for all ranges of interest. Such a method, however, raises the computational complexity compared with the standard stretch processing as it obtains the range information via matrix multiplication instead of fast Fourier transform (FFT). To lower the computationally complexity, the dechirping and decoding receiver for PC-FMCW has been proposed in [21] and [22]. There the dechirping is followed by the alignment of the coded beat signals for targets at different ranges using an ideal group delay filter. After alignment, all coded beat signals are decoded with the reference code, and the target range information is extracted from the beat signals via FFT. However, the group delay filter causes a quadratic phase shift (group delay dispersion effect) on the dechirped signal, resulting in the distortion of the code present in that signal. Consequently, the decoding becomes imperfect, which raises the sidelobes in the range profile.

The most popular phase coding scheme used for PC-FMCW in the preliminary studies [21], [25] was binary phase shift keying (BPSK). The BPSK coding causes abrupt phase changes that lead to a large spectrum widening of the beat signal. As a consequence, the BPSK signal only with a small bandwidth compared with the sampling frequency (a few chips per chirps) can be used for sensing [24]. In the case of BPSK code bandwidth being comparable to the sampling frequency of ADC, the sidelobe level significantly increases. Therefore, other phase modulation types with lower spectral broadening and, thus, better sensing performance are still of much interest.

In this article, we have studied smoothed phase-coded frequency-modulated continuous waveform (SPC-FMCW) to enhance the coexistence of multiple radars, and we have investigated the receiving strategy with a low ADC sampling requirement. The phase smoothing operation is proposed to obtain a smooth phase transition that addresses the bandwidth limitations of BPSK, and then, the phase lag compensation is applied to the transmitted phase code to eliminate the undesired effect of the group delay filter. For analysis, we have used the Gaussian filter as a smoother and derived the waveform in different domains. Subsequently, we have investigated the waveform properties analytically. In addition, we have applied the proposed waveform to a real scenario and examined its sensing performance experimentally.

The rest of this article is organized as follows. Section II describes the signal model for the generic PC-FMCW and gives the transceiver structure for the signal. Section III presents a smoothing operation to improve the phase transition of PC-FMCW. Section IV provides the phase lag compensation, and Section V investigates waveform properties of the resulting waveforms. Section VI demonstrates the application of the waveforms to a real scenario. Finally, Section VII concludes this article.

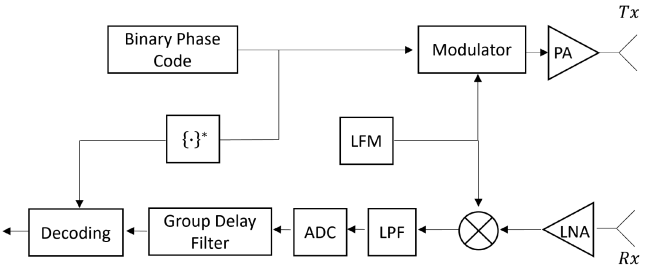

Fig. 1. Block diagram of the state-of-the-art PC-FMCW transceiver structure.

II. SIGNAL MODEL AND TRANSCEIVER STRUCTURE

This section introduces the signal model and the state-of-the-art transceiver structure of PC-FMCW [21], as shown in Fig. 1.

The transmitted signal for frequency-modulated continuous waveform (FMCW) can be written as

$$x_{\mathrm{FMCW}}(t) = e^{-j(2\pi f_c t + \pi k t^2)}, \quad t \in [0,\ T] \tag{1}$$

where f_c is the carrier frequency, T is the sweep duration of the signal, $k = B/T$ is the slope of the linear frequency-modulated waveform, and B is the bandwidth. In PC-FMCW, the phase of FMCW changes according to the code sequence. The transmitted signal for the PC-FMCW radar can be represented as

$$x_{\mathrm{T}}(t) = s(t)e^{-j(2\pi f_c t + \pi k t^2)} \tag{2}$$

where $s(t)$ is a phase-coded[1] signal. The received signal reflected from a moving point-like target can be written as

$$x_{\mathrm{R}}(t) = \alpha_0\, s(t - \tau(t))e^{-j\left(2\pi f_c(t-\tau(t)) + \pi k(t-\tau(t))^2\right)} \tag{3}$$

where α_0 is a complex amplitude proportional to the target back-scattering coefficient and propagation effects. Hereinafter, we substitute all the constant terms in α_0 with no loss of generality. The round trip delay $\tau(t)$ for a target with constant velocity can be represented as

$$\tau(t) = \frac{2(R_0 + v_0 t)}{c} = \tau_0 + \frac{2v_0 t}{c} \tag{4}$$

where R_0 is the range, v_0 is the velocity, and c is the speed of light. The range and velocity information of the target can be obtained by extracting the $\tau(t)$ from the received signal. In the state-of-the-art transceiver structure, the received signal is mixed with the complex conjugate of the uncoded transmit signal (1) for dechirping process [21]. The complex mixer output can be written as

$$\begin{aligned} x_{\mathrm{M}}(t) &= x_{\mathrm{R}}(t)x^*_{\mathrm{FMCW}}(t) \\ &= \alpha_0\, s(t - \tau(t))e^{j(2\pi f_c\tau(t) + 2\pi k\tau(t)t - \pi k\tau(t)^2)} \\ &= \alpha_0\, s\left(t - \tau_0 - \frac{2v_0 t}{c}\right) e^{j(2\pi f_c\tau_0 + 2\pi f_d t + 2\pi f_b t)} \end{aligned} \tag{5}$$

[1]The phase code signal can also be kept inside the exponent as a phase term. We choose to write phase coding term as a separate signal component for more generic representation and ease of following.

where $(\cdot)^*$ denotes the complex conjugate, $f_d = \frac{2v_0 f_c}{c}$ is the Doppler frequency, and f_b is the beat frequency defined as

$$f_b = k\tau_0. \tag{6}$$

Since the velocity of the target is much smaller than the speed of light as $v_0 \ll c$, the delayed code term can be approximated as $s(t - \tau_0 - \frac{2v_0 t}{c}) \approx s(t - \tau_0)$. Moreover, $e^{j(2\pi f_c \tau_0)}$ is a constant phase term and, thus, incorporated into α_0.

In automotive radars, the Doppler frequency of the target is typically negligible compared with the frequency resolution of the beat signal, i.e., $f_d \ll f_s/N$, where f_s is the sampling frequency of the beat signal and N is the number of fast-time samples. Thus, we can approximate the $f_d + f_b \approx f_b$ without loss of generality. Note that we only neglected the Doppler frequency shift associated with fast-time, and there will be an additional term $\exp(2\pi f_d mT)$ for velocity estimation in slow-time processing, where m is the number of pulses. Since the group delay filter and decoding are only related to the fast-time processing part, we focus on signal analysis in fast-time. The slow-time processing is straightforward and the same as in the conventional FMCW automotive radars. Consequently, the mixer output in fast-time can be written as

$$x_{\mathrm{M}}(t) = \alpha_0\, s(t - \tau_0) e^{j(2\pi f_b t)}. \tag{7}$$

By taking the Fourier transform, the frequency-domain representation of the mixer output can be obtained as

$$\begin{aligned} X_{\mathrm{M}}(f) &= \alpha_0 \int_{-\infty}^{\infty} s(t - \tau_0) e^{j(2\pi f_b t)} e^{-j2\pi f t}\, dt \\ &= \alpha_0 e^{-j(2\pi(f - f_b)\tau_0)} \int_{-\infty}^{\infty} s(t_1) e^{-j(2\pi(f - f_b)t_1)}\, dt_1 \\ &= \alpha_0 S(f - f_b) e^{-j\left(2\pi(f - f_b)\tau_0\right)} \\ &= \alpha_0 S(f - f_b) e^{-j\left(\frac{2\pi f_b}{k}(f - f_b)\right)} \end{aligned} \tag{8}$$

where for the final equality we used (6).

In the decoding process, the mixer output (7) is multiplied with the complex conjugate of the reference phase code for compensating phase changes initiated by the transmitted phase code. For a short-range radar application, e.g., indoor monitoring, the delay can be neglected $s(t - \tau_0) \approx s(t)$, and the mixer output can be decoded by multiplying (7) with $s^*(t)$ directly [24]. However, this assumption does not hold for the applications with $R \geq c/(2B_c)$, where B_c is the bandwidth of phase-coded signal $s(t)$. For these applications, each coded beat signal (the response in all the range cells) is required to be aligned in fast-time to compensate the time delay before decoding. This alignment can be realized via the group delay filter either in time domain [21], or frequency domain [22]. Assume that we have a group delay filter with frequency response

$$H_{\mathrm{g}}(f) = |H_{\mathrm{g}}(f)| \angle H_{\mathrm{g}}(f) = e^{j\theta_g(f)} \tag{9}$$

and unity magnitude $|H_{\mathrm{g}}(f)| = 1 \forall f$.

The Taylor series expansion of the phase response $\theta_g(f)$ around f_b can be found as

$$\begin{aligned} \theta_g(f)\big|_{f=f_b} &= \theta(f_b) + \frac{d\theta(f)}{df}\Big|_{f=f_b} (f - f_b) \\ &\quad + \sum_{m=2}^{\infty} \frac{1}{m!} \frac{d^m \theta(f)}{df^m}\Big|_{f=f_b} (f - f_b)^m. \end{aligned} \tag{10}$$

The resulting filter causes the group delay, $\tau_g(f)$, which is the first derivative of the phase response and shifts the envelope of the signal (the proof is given in Appendix C). To align coded beat signals, the group delay needs to eliminate τ_0. Thus, the required group delay can be found as

$$\tau_{\mathrm{g}}(f) = -\frac{1}{2\pi} \frac{d\theta(f)}{df}\Big|_{f=f_b} = -\tau_0 = -f_b/k \tag{11}$$

and consequently, the first derivative of the phase response can be written as

$$\frac{d\theta(f)}{df}\Big|_{f=f_b} = \frac{2\pi f_b}{k}. \tag{12}$$

The group delay filter which gives the required group delay in (12) can be written as

$$H_{\mathrm{g}}(f) = e^{j\theta_g(f)} = e^{j\frac{\pi f^2}{k}}. \tag{13}$$

We apply the group delay filter by multiplying the spectrum of mixer output as

$$Z_{\mathrm{o}}(f) = X_{\mathrm{M}}(f) H_{\mathrm{g}}(f). \tag{14}$$

For each beat frequency, the frequency characteristic of the group delay filter can be expressed by the Taylor series expansion of its phase response around f_b as

$$\theta_g(f)\big|_{f=f_b} = \frac{\pi {f_b}^2}{k} + \frac{2\pi f_b}{k}(f - f_b) + \frac{\pi}{k}(f - f_b)^2. \tag{15}$$

Subsequently, multiplying the mixer output spectrum with the frequency characteristic of the filter gives

$$\begin{aligned} Z_{\mathrm{o}}(f) &= X_{\mathrm{M}}(f) e^{j\left(\frac{\pi {f_b}^2}{k} + \frac{2\pi f_b}{k}(f - f_b) + \frac{\pi}{k}(f - f_b)^2\right)} \\ &= \alpha_0 S(f - f_b) e^{-j\left(\frac{2\pi f_b}{k}(f - f_b)\right)} \\ &\quad \cdot e^{j\left(\frac{\pi {f_b}^2}{k} + \frac{2\pi f_b}{k}(f - f_b) + \frac{\pi}{k}(f - f_b)^2\right)} \\ &= \alpha_0 S(f - f_b) e^{j\left(\frac{\pi {f_b}^2}{k} + \frac{\pi}{k}(f - f_b)^2\right)} \\ &= \alpha_0 S(f - f_b) e^{j\left(\frac{\pi}{k}(f - f_b)^2\right)} \end{aligned} \tag{16}$$

where for the last equality we incorporated $\exp(\frac{\pi {f_b}^2}{k})$ into α_0 as it is a constant phase term (does not depend on frequency f). Then, taking the inverse Fourier transform of the group delay filter output (16) gives

$$\begin{aligned} z_{\mathrm{o}}(t) &= \mathcal{F}^{-1}\left\{\alpha_0 S(f - f_b) e^{j\left(\frac{\pi}{k}(f - f_b)^2\right)}\right\} \\ &= \mathcal{F}^{-1}\left\{\alpha_0 S(f - f_b)\right\} \otimes \mathcal{F}^{-1}\left\{e^{j\left(\frac{\pi}{k}(f - f_b)^2\right)}\right\} \\ &= \left(\alpha_0 s(t) e^{j(2\pi f_b t)}\right) \otimes \mathcal{F}^{-1}\left\{e^{j\left(\frac{\pi}{k}(f - f_b)^2\right)}\right\} \end{aligned} \tag{17}$$

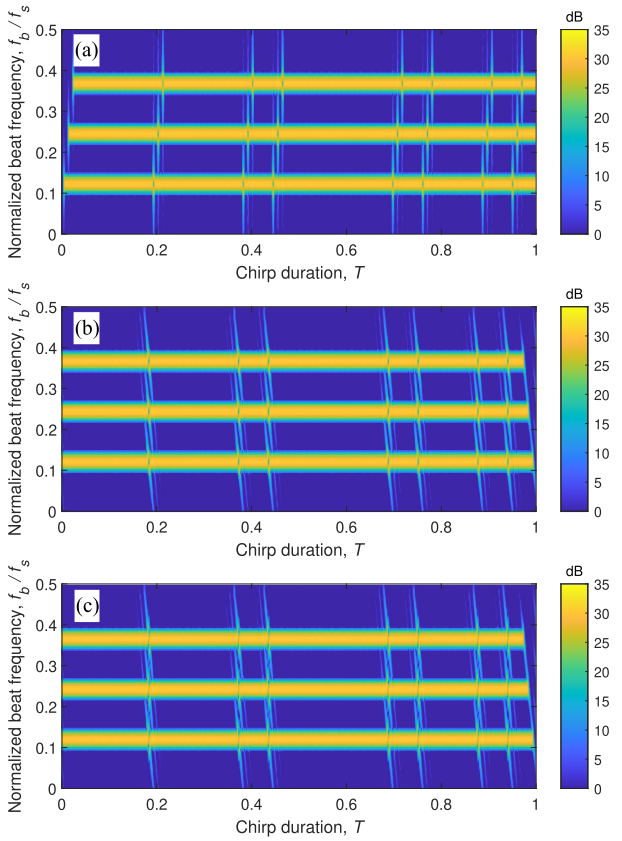

Fig. 2. Spectrogram of the BPSK phase-coded beat signals ($N_c = 16$). (a) Before the group delay filter. (b) After the group delay filter. (c) After decoding the group delay filter output.

where $\otimes$ denotes the convolution operation. Note that the delay τ_0 is eliminated after the group delay filter for each coded beat signal. Moreover, the derived group delay filter has a quadratic frequency component within its phase response and applies different time delays to each frequency component. Consequently, the filter causes the so-called group delay dispersion effect shown as term $e^{j(\frac{\pi}{k}(f-f_b)^2)}$, which leads to a nonlinear shift on the spectrum of the code signal. By substituting $\zeta = -j\frac{\pi}{k}$ and $f_1 = f - f_b$, the dispersion effect can be written as

$$\begin{aligned} h_{\text{dis}}(t) &= \mathcal{F}^{-1}\left\{e^{j(\frac{\pi}{k}(f-f_b)^2)}\right\} \\ &= \int_{-\infty}^{\infty} e^{-\zeta {f_1}^2}\, e^{j2\pi f_1 t}\, df_1\, e^{j2\pi f_b t} \\ &= e^{j2\pi f_b t}\, e^{-\frac{\pi^2 t^2}{\zeta}} \int_{-\infty}^{\infty} e^{-\left(\sqrt{\zeta} f_1 - j\frac{\pi t}{\sqrt{\zeta}}\right)^2} df_1 \\ &= \sqrt{-\frac{k}{j}}\, e^{\pi \frac{kt^2}{j}}\, e^{j2\pi f_b t}. \end{aligned} \tag{18}$$

Subsequently, the mixer output in time domain (17) can be recast as

$$z_{\text{o}}(t) = \alpha_0\, e^{j2\pi f_b t}\ (s(t) \otimes h_{\text{dis}}(t))\,. \tag{19}$$

The spectrogram of the BPSK phase-coded beat signals is shown in Fig. 2, where the system parameters are selected as $B = 2\,\text{GHz}, T = 51.2\,\mu\text{s}$, and $N_c = 16$. Subsequently, the code bandwidth $B_c = \frac{N_c}{T} = 0.31$ MHz with these parameters ($N_c = 16$). We use the same system parameters for the follow-up figures, if not mentioned, otherwise. Moreover, we normalize the beat frequency with the maximum beat frequency, which is determined by the ADC sampling frequency as $f_{b_{\max}} = f_s/2$. In Fig. 2, we compare three cases: before the group delay filter, after the group delay filter, and after decoding the group delay filter output. It can be seen that each coded beat signal has different time delays (associated with their corresponding range) before the group delay filter, see Fig. 2(a). After using the group delay filter, we observe that each coded beat signal is aligned at the beginning, see Fig. 2(b). Note that the signals with a lower frequency are shifted less compared with signals with higher frequency. As a result of coded beat signal alignment, the decoding can be performed by multiplying the group delay filter output with the complex conjugate of the reference phase code. In an ideal decoding, the multiplication of codes gives $s(t)s^*(t) = e^{j\phi(t)}e^{-j\phi(t)} = 1$. However, the spectrum of the code signal is shifted nonlinearly [see Fig. 2(b)] as it is convolved with $h_{\text{dis}}(t)$. Thus, decoding becomes imperfect, and the code term is not removed properly, see Fig. 2(c). The decoded beat signal can be written as [22]

$$\begin{aligned} z_{\text{d}}(t) &= z_{\text{o}}(t)s^*(t) \\ &= \alpha_0 e^{j2\pi f_b t}\ (s(t) \otimes h_{\text{dis}}(t))\ s^*(t) \\ &= \alpha_0 e^{j2\pi f_b t}\ \left(e^{j\phi(t)} \otimes h_{\text{dis}}(t)\right)\ e^{-j\phi(t)} \\ &= \alpha_0 e^{j2\pi f_b t}\ e^{j\epsilon(t)} \end{aligned} \tag{20}$$

where $\epsilon(t)$ is the residual phase error due to the group delay filter dispersion that causes imperfection in decoding. The dispersion effect can be neglected for a narrow-band signal where the bandwidth of the phase-coded signal is very small compared with the sampling frequency $B_c \ll f_s$. However, the dispersion effect becomes crucial for a signal with a wide spectrum where B_c is comparable to f_s. One example of such a signal is the BPSK phase-coded beat signal. In the time instance of phase shifts, the BPSK signal has a wide-spread spectrum due to abrupt phase changes. Applying nonlinear phase shifts to its spectrum leads to huge imperfection in decoding. Consequently, the BPSK signal suffers from the distorted range profile after decoding, as shown in Fig. 3, where we use $N_c = 64$. The distortion of the range profile raises for the long code sequences (the bandwidth of the chips increase). We will address the compensation of the

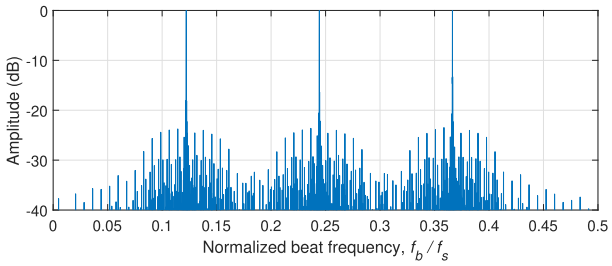

Fig. 3. Distorted range profile of decoded signal after the group delay filter ($N_c = 64$).

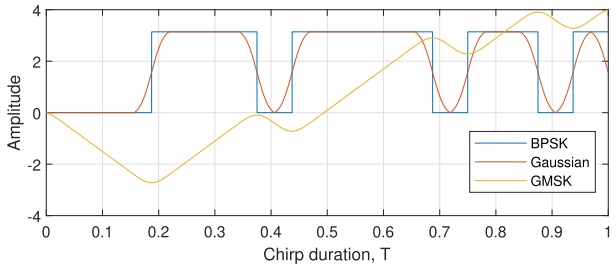

Fig. 4. Illustration of the phase types ($N_c = 16$): BPSK, Gaussian, and GMSK.

group delay dispersion effect by applying quadratic phase lag to the waveform before transmission in Section IV.

III. SMOOTH PHASE TRANSITION WAVEFORMS

This section presents the smoothing operation to improve the phase transition of the state-of-the-art waveform and reduces its spectral widening of the coded beat signal to obtain SPC-FMCW.

A. BPSK PC-FMCW

In BPSK, the phase changes $\phi_{\text{bpsk}}(t) \in \{0, \pi\}$, as shown in Fig. 4, and the transmitted code term can be represented as

$$c(t) = e^{j\phi_{\text{bpsk}}(t)} = \frac{1}{T}\frac{1}{T_c}\sum_{n=1}^{N_c} e^{j\phi_n}\text{rect}\left(\frac{t-(n-1/2)T_c}{T_c}\right) \tag{21}$$

where N_c is the number of chips within one chirp, $T_c = T/N_c$ is the chip duration, $\text{rect}(t) = 1, t \in [-T_c/2,\ T_c/2]$, and zero, otherwise, is the rectangle function, and ϕ_n denotes the phase corresponding to the n^{th} bit of the N_c bits sequence.

In addition, analyzing the spectrogram of the phase-coded signal is complementary as it provides an additional perspective that may not easily be seen on the signal's time or frequency domain representation. The instantaneous frequency for the BPSK code sequence can be written as [25]

$$\frac{1}{2\pi}\frac{d}{dt}\phi_{\text{bpsk}}(t) = \frac{1}{2\pi}\sum_{n=1}^{N_c}(\phi_{n+1}-\phi_n)\delta(t-nT_c). \tag{22}$$

The proof is given in Appendix A. The instantaneous frequency of BPSK is demonstrated in Fig. 5(a). It can be seen that the abrupt phase changes cause a short burst in the spectrum at the time instances of phase shifts, which mathematically comes from the derivatives of unit step functions and is represented as Dirac delta in (22).

For BPSK PC-FMCW, we can replace the $s(t-\tau_0)$ term with $c(t-\tau_0)$, and the mixer output becomes

$$x_{\text{M}_{\text{bpsk}}}(t) = \alpha_0 c(t-\tau_0)e^{j(2\pi f_b t)} \tag{23}$$

and the frequency-domain representation of the mixer output can be written as

$$X_{\text{M}_{\text{bpsk}}}(f) = \alpha_0 C(f-f_b)e^{-j(2\pi(f-f_b)\tau_0)}$$

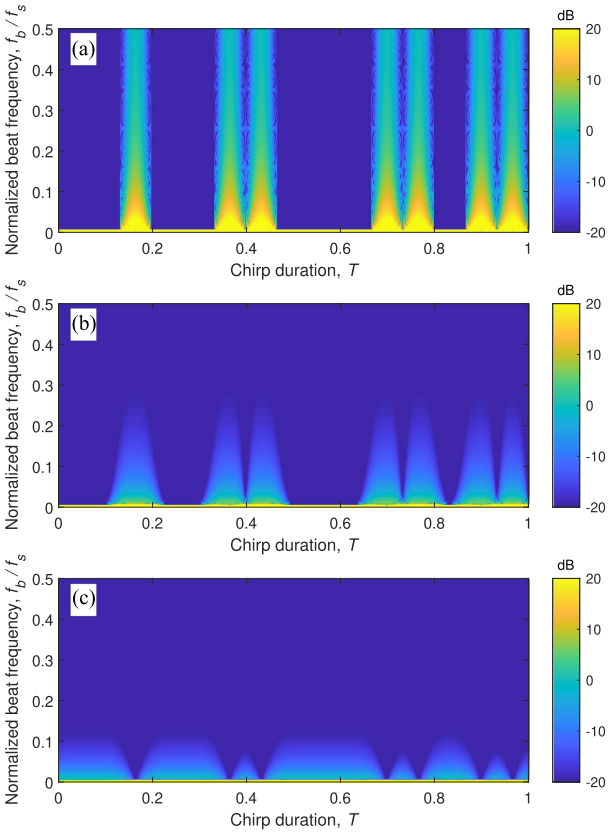

Fig. 5. Instantaneous frequency of the coded beat frequency signal associated with three PC-FMCW waveforms ($N_c = 16$). (a) BPSK. (b) Gaussian. (c) GMSK.

$$= \frac{\alpha_0}{T}\sum_{n=1}^{N_c} e^{j\phi_n}\text{sinc}((f-f_b)T_c)e^{-j\left(2\pi(f-f_b)(\tau_0+(n-\frac{1}{2})T_c)\right)}. \tag{24}$$

The frequency spectrum of the mixer output (24) with $\tau_0 = 0$ is shown in Fig. 6 in blue color. The first null for the mixer output of BPSK PC-FMCW is defined by the sinc function, as shown in (24). Therefore, the first null location of the coded beat signal for BPSK PC-FMCW can be calculated as

$$f_b + B_c \tag{25}$$

where $B_c = 1/T_c$ is the bandwidth of chip. Assume that we have an ideal Brick-wall low-pass filter (LPF) as

$$L(f) = \text{rect}\left(\frac{f}{f_{\text{cut}}}\right). \tag{26}$$

The output of the LPF can be represented as

$$O(f) = X_{\text{M}}(f)L(f). \tag{27}$$

To include the kth null, the cutoff frequency of LPF can be written as

$$f_{\text{cut}} \geq f_{b_{\max}} + \frac{1}{T_c}k\text{th}_{\text{null}}$$
$$\geq f_{b_{\max}} + \frac{N_c}{T}k\text{th}_{\text{null}}$$

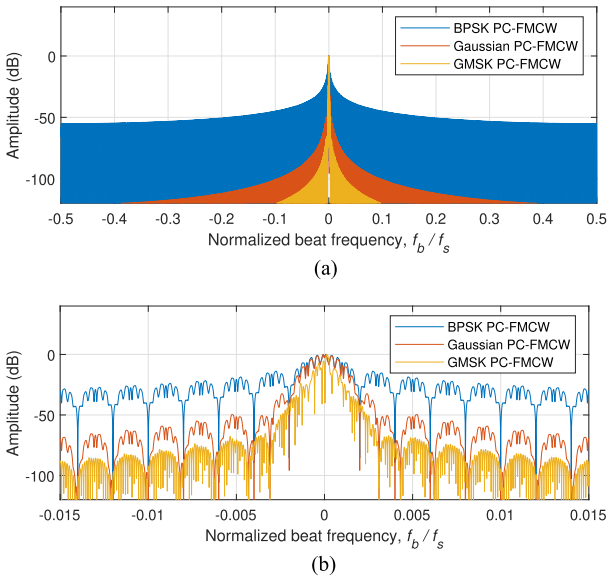

Fig. 6. Frequency spectrum comparison for the coded beat signals associated with three PC-FMCW waveforms with $N_c = 16$. (a) Full-band. (b) Zoomed.

$$\geq k\tau_{\max} + \frac{N_c}{T} k\text{th}_{\text{null}}$$
$$\geq \frac{1}{T}\left(\frac{2BR_{max}}{c} + N_c k\text{th}_{\text{null}}\right). \tag{28}$$

where $f_{b_{\max}} = k\tau_{\max}$ is the maximum beat frequency and $\tau_{\max} = 2R_{\max}/c$ is the maximum round trip delay for the stationary target at the maximum range $R_{\max}$. The cutoff frequency of LPF determines the minimum ADC sampling requirement, which should be at least two times of f_{cut}. The BPSK coding results in substantial spectrum widening of the beat signal due to rapid phase shifts. Thus, the BPSK coding requires the sampling of a few multiples of code bandwidth. The spectrum width of a signal $x(t)$ can be calculated as [26]

$$\sigma_{\text{f}} = \sqrt{\frac{1}{\text{P}}\int_{-\infty}^{\infty}(f-\mu_f)^2\,|X(f)|^2\,df} \tag{29}$$

where the total power of the spectrum can be defined as

$$\text{P} = \int_{-\infty}^{\infty}|X(f)|^2\,df \tag{30}$$

and the mean frequency of the spectrum can be written as

$$\mu_f = \frac{1}{\text{P}}\int_{-\infty}^{\infty} f\,|X(f)|^2\,df. \tag{31}$$

The spectrum width of the coded beat signals associated with three PC-FMCW waveforms versus number of chips per chirp is shown in Fig. 7. It can be seen that the spectrum widening of the coded beat signal increases as the number of chips per chirp raises (code bandwidth becomes larger, e.g., the normalized code bandwidth becomes $B_c/f_s = 0.12$ for $N_c = 1024$ and $f_s = 160$ MHz). Using the BPSK code with large bandwidth comparable to the sampling frequency and

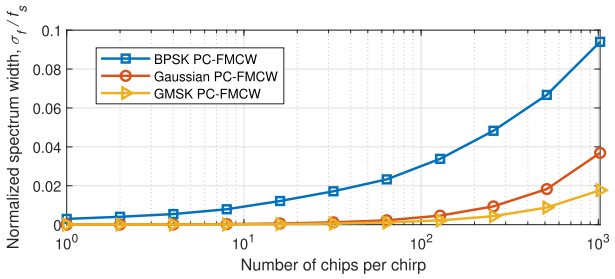

Fig. 7. Spectrum width of the coded beat signals associated with three PC-FMCW waveforms versus number of chips per chirp. Normalized code bandwidth $B_c/f_s = 0.12$ for $N_c = 1024$.

filtering of the spectrum leads to increased sidelobe level. To cope with this problem, we can apply a smoother.

B. Gaussian PC-FMCW

A smoother can be applied to the phase of the code signal to reduce the spectrum widening of the coded beat signal. In this article, we have used the Gaussian filter as a smoother for analysis. However, a different smoothing filter can be selected depending on the required spectral behavior of the application. The Gaussian filter can be represented as

$$h(t) = \sqrt{\frac{2\pi}{\ln 2}}B_s e^{-\frac{2\pi^2 B_s^2}{\ln 2}t^2}$$
$$= \frac{\eta}{\sqrt{\pi}}e^{-\eta^2 t^2} \tag{32}$$

where $\eta = \sqrt{\frac{2\pi^2 B_s^2}{\ln 2}}$ and B_s is the 3-dB bandwidth of the Gaussian filter. The Gaussian filter in frequency domain can be written as [27]

$$H(f) = e^{-\frac{\ln(2)}{2}\left(\frac{f}{B_s}\right)^2}. \tag{33}$$

Applying Gaussian filter to the binary code, we obtained the Gaussian binary code $\phi_{\text{gauss}}(t) = \phi_{\text{bpsk}}(t) \otimes h(t)$, as demonstrated in Fig. 4. The instantaneous frequency for the Gaussian binary code can be written as

$$\frac{1}{2\pi}\frac{d}{dt}\phi_{\text{gauss}}(t) = \frac{\eta}{2\pi\sqrt{\pi}}\sum_{n=1}^{N_c}(\phi_{n+1}-\phi_n)e^{-\eta^2(t-nT_c)^2}. \tag{34}$$

The proof is given in Appendix A. Equation (34) shows that the abrupt phase changes are smoothed by the Gaussian filter, and the term $e^{-\eta^2(t-nT_c)^2}$ is expected when the phase changes with respect to time. This can be seen in Fig. 5(b) that the phase changes cause Gaussian shape in the instantaneous frequency of the Gaussian binary code.

In addition, the mixer output of Gaussian PC-FMCW can be represented as

$$x_{\text{M}_{\text{gauss}}}(t) = \alpha_0\,(c(t-\tau_0) \otimes h(t-\tau_0))\,e^{j(2\pi f_b t)} \tag{35}$$

and its frequency spectrum can be written as

$$X_{\text{M}_{\text{gauss}}}(f) = \alpha_0 C(f-f_b)\,H(f-f_b)\,e^{-j(2\pi(f-f_b)\tau_0)}$$

$$= \frac{\alpha_0}{T}\sum_{n=1}^{N_c} e^{j\phi_n}\text{sinc}((f-f_b)T_c)$$
$$e^{-j\left(2\pi(f-f_b)\left(\tau_0+\left(n-\frac{1}{2}\right)T_c\right)\right)}\, e^{-\frac{\ln(2)}{2}\left(\frac{f-f_b}{B_s}\right)^2}. \quad (36)$$

As seen in (36), the first null of the mixer output for the Gaussian PC-FMCW is decided by the sinc function bounded by the Gaussian filter $H(f)$. Consequently, the first null location becomes $f_b + B_s$, and the required cutoff frequency to include the main lobe becomes

$$f_{\text{cut}} \geq f_{b_{\max}} + B_s. \quad (37)$$

The frequency spectrum of the mixer output for Gaussian PC-FMCW (36) is demonstrated in Fig. 6 in red color. We observe that using a Gaussian filter reduces the spectrum widening of the coded beat signal. This can be seen in Fig. 7 where the spectrum width of the coded beat signal is lowered for Gaussian PC-FMCW compared with the BPSK coded signal.

C. Gaussian Minimum Shift Keying (GMSK) PC-FMCW

GMSK is a popular modulation scheme in communication due to its low spectral spread. In GMSK, the binary code signal is filtered by a Gaussian filter, and the filtered code is integrated over time [28], [29]. The resulting phase for GMSK becomes $\phi_{\text{gmsk}}(t) = \int_{-\infty}^{\infty}\phi_{\text{gauss}}(t)dt = \int_{-\infty}^{\infty}(\phi_{\text{bpsk}}(t) \otimes h(t))dt$, as shown in Fig. 4. The instantaneous frequency for the GMSK phase code can be obtained as

$$\frac{1}{2\pi}\frac{d}{dt}\phi_{\text{gmsk}}(t) = \frac{1}{4\pi}\sum_{n=1}^{N_c}(\phi_{n+1}-\phi_n)\,\text{erf}\,(\eta(t-nT_c)) \quad (38)$$

where erf (t) represents the error function. The proof is given in Appendix A. Equation (38) demonstrates that the Dirac delta term seen in BPSK coding due to abrupt phase change is replaced by the term $\text{erf}\,(\eta(t-nT_c))$ for the GMSK phase code. This behavior can be observed in Fig. 5(c), where the phase changes lead to error functions (combination of left and right parts gives a smoothed rectangle shape) in the instantaneous frequency of the GMSK phase code.

Subsequently, the mixer output of GMSK PC-FMCW can be represented as

$$x_{\text{M}_{\text{gmsk}}}(t) = \alpha_0 e^{j\phi_{\text{gmsk}}(t-\tau_0)}e^{j(2\pi f_b t)} \quad (39)$$

and its frequency-domain representation can be written as [27]

$$X_{\text{M}_{\text{gmsk}}}(f) \approx \frac{\alpha_0}{T}\sum_{n=1}^{N_c} e^{j\phi_n}\text{sinc}^2((f-f_b)T_c)$$
$$e^{-j2\pi(f-f_b)(\tau(t)+(n-1/2)T_c)}\, e^{-\frac{\ln(2)}{2}\left(\frac{f-f_b}{B_s}\right)^2}. \quad (40)$$

Similar to the Gaussian case, the Gaussian filter $H(f)$ bounds the frequency components of the mixer output for GMSK PC-FMCW, as shown in (40). Thus, the first null location becomes $f_b + B_s$, and the required cutoff frequency to include the main lobe is the same as (37). In addition, GMSK PC-FMCW has a sinc^2 term instead of a sinc function, which is seen in the BPSK code. This is because the GMSK phase code has a smoothed triangular shape while BPSK has rectangular, as shown in Fig. 4.

The frequency spectrum of the mixer output for GMSK PC-FMCW (40) is shown in Fig. 6 in yellow color. It can be seen that taking the square of the sinc function and bounding it by the Gaussian filter further reduces the spectrum widening of the coded beat signal. We observe this in Fig. 7 as the spectrum width of the coded beat signal associated with GMSK PC-FMCW is lower (especially for a large code bandwidth) compared with both BPSK PC-FMCW and Gaussian PC-FMCW. Consequently, better sensing performance (i.e., lower sidelobe level) is expected for a GMSK PC-FMCW when the bandwidth of the code increases and becomes comparable to ADC sampling.

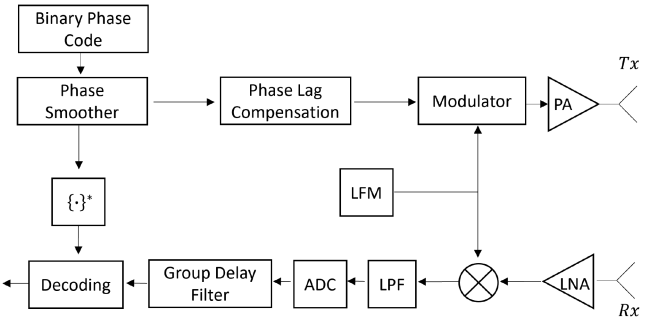

Fig. 8. Block diagram of the proposed PC-FMCW transceiver structure.

IV. PHASE LAG COMPENSATED WAVEFORMS

This section introduces the phase lag compensated waveforms, and the proposed block diagram is shown in Fig. 8. The signals that are modified due to the implementation of the phase lag compensation are denoted with a symbol (̂).

The group delay filter applies different time delays to each frequency component and causes a dispersion effect on the phase-coded signal, which leads to a distorted range profile, as explained in Section II. To eliminate the undesired effect of the group delay filter, we perform quadratic phase lag compensation on the transmitted code by multiplying its spectrum with the quadratic phase term as [30]

$$\hat{S}(f) = S(f)e^{-j\frac{\pi f^2}{k}}. \quad (41)$$

Then, the mixer output (7) becomes

$$\hat{x}_{\text{M}}(t) = \alpha_0\hat{s}(t-\tau_0)e^{j(2\pi f_b t)} \quad (42)$$

and

$$\hat{X}_{\text{M}}(f) = \alpha_0 S(f-f_b)e^{-j\left(\frac{2\pi f_b}{k}(f-f_b)+\frac{\pi}{k}(f-f_b)^2\right)} \quad (43)$$

for time and frequency domain representation, respectively. Subsequently, the output of the group delay filter in the frequency domain becomes

$$\hat{Z}_{\text{o}}(f) = \hat{X}_{\text{M}}(f)e^{j\left(\frac{\pi {f_b}^2}{k}+\frac{2\pi f_b}{k}(f-f_b)+\frac{\pi}{k}(f-f_b)^2\right)}$$

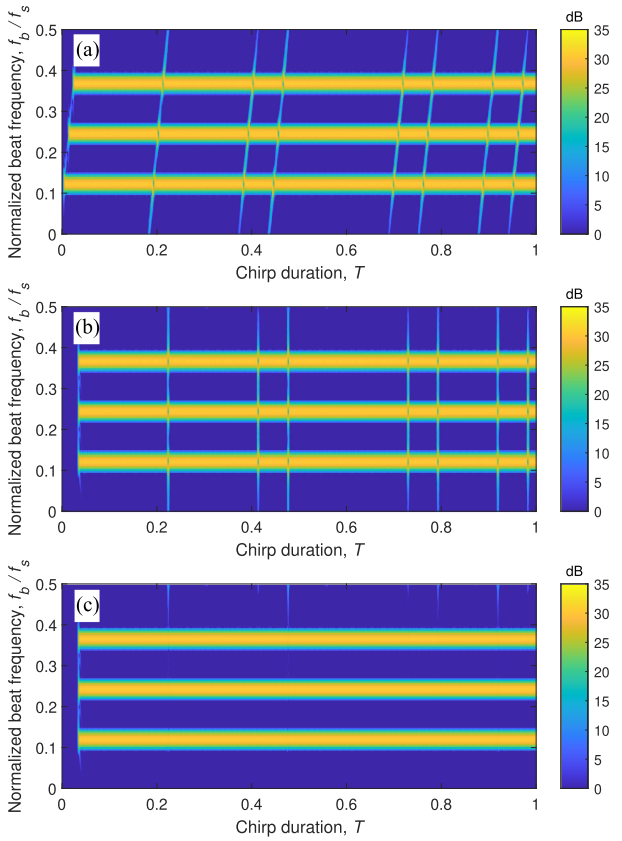

Fig. 9. Spectrogram of the BPSK phase-coded beat signals ($N_c = 16$) with phase lag compensation applied. (a) Before the group delay filter. (b) After the group delay filter. (c) After decoding the group delay filter output.

$$= \alpha_0 S(f - f_b) e^{j\left(\frac{\pi f_b^2}{k}\right)}$$
$$= \alpha_0 S(f - f_b) \tag{44}$$

where $\exp(\frac{\pi f_b^2}{k})$ is a constant phase term (does not depend on frequency f), and thus, it can be incorporated into α_0. Note that the undesired term $\frac{\pi}{k}(f - f_b)^2$ caused by the phase response of the filter (15) is eliminated with the phase lag compensation. After taking the inverse Fourier transform, the time domain representation of the new group delay filter output (44) becomes

$$\hat{z}_o(t) = \alpha_0 s(t) e^{j(2\pi f_b t)}. \tag{45}$$

In addition, we can shift the group delay filter output to the maximum delay (defined by maximum beat frequency, $\tau_{\max} = \frac{f_{b\max}}{k}$) by multiplying its spectrum with linear phase delay $\exp(-j2\pi f \tau_{\max})$ for physical correctness and guarding the beginning of the next chirp. Consequently, (45) is shifted to the maximum time delay as

$$z_a(t) = \alpha_0 s\,(t - \tau_{\max})\, e^{j(2\pi f_b t)}. \tag{46}$$

The spectrogram of the BPSK phase-coded beat signals with phase lag compensation applied is shown in Fig. 9 ($B = 2$ GHz, $T = 51.2$ μs, and $N_c = 16$) for three cases: before the group delay filter, after the group delay filter, and after decoding the group delay filter output. Note that

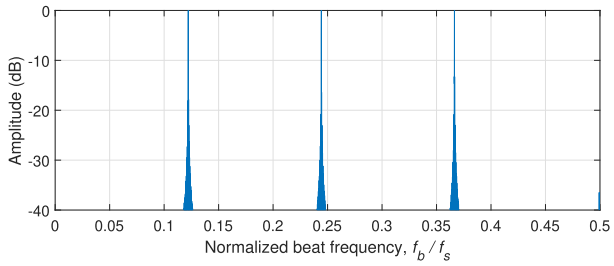

Fig. 10. Recovered range profile of decoded signal after using phase lag compensation and group delay filter ($N_c = 64$).

by using phase lag compensation, the spectrum of the code signals is nonlinearly shifted in the opposite direction before applying the group delay filter Fig. 9(a). An example of the resulting signal (46) can be seen in Fig. 9(b). It is observed that the group delay dispersion effect on the code signal is eliminated, and each coded beat signal is perfectly aligned after the group delay filter. Subsequently, we can apply the decoding signal, which is the complex conjugate of the reference phase code shifted to maximum beat frequency, and the decoded beat signal becomes

$$\hat{z}_d(t) = z_a(t) s^*\,(t - \tau_{\max})$$
$$= \alpha_0 e^{j(2\pi f_b t)}. \tag{47}$$

It can be seen in (47) that the code term is removed properly, and the residual phase error caused by the imperfection in decoding is eliminated by using the phase lag compensation, see Fig. 9(c). As a consequence, the distorted range profile shown in Fig. 3 is recovered for a wideband signal where B_c is comparable to f_s, as illustrated in Fig. 10. Moreover, the beat signals are obtained similar to the dechirped signal of conventional FMCW radar. This helps reutilizing all software algorithms previously developed for FMCW radar with the proposed waveform and transceiver structure.

V. WAVEFORM PROPERTIES

This section provides the properties of the phase lag compensated PC-FMCW. For the numerical simulations, we consider a radar operating with a carrier frequency $f_c = 3.315$ GHz and transmitting the investigated waveforms with the chirp duration $T = 1$ ms and the chirp bandwidth $B = 200$ MHz. The phase lag compensated signal $\hat{s}(t)$ is used for phase coding, and we have used the random code sequence for all three PC-FMCW. The duration of the chip T_c is controlled with the number of chips per chirp N_c as $T_c = T/N_c$. To achieve a smoothed phase transition, the 3-dB bandwidth of the Gaussian filter is set to two times the chip bandwidth $B_s = 2B_c$. On the receiver side, (42) is low-pass filtered with the cutoff frequency $f_{\text{cut}} = \pm 20$ MHz and sampled with $f_s = 40$ MHz. As a consequence, we have $N = 40\,000$ range cells (fast-time samples) for this setting. The group delay filter is applied to the sampled signal to align the beat signals of different targets. Before decoding, the same LPF is applied to the reference phase-coded signal to prevent a signal mismatch. To focus on the waveform

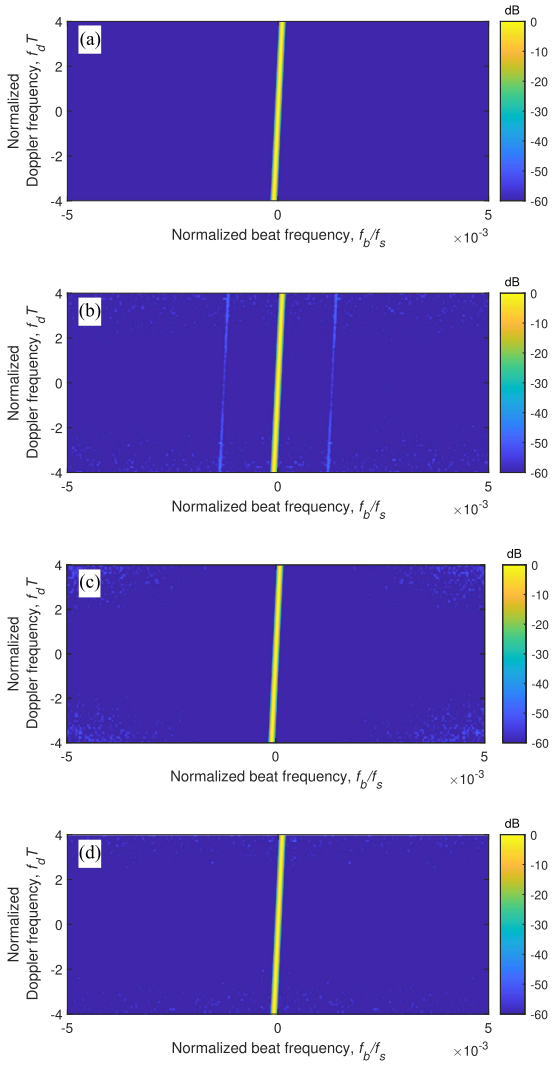

Fig. 11. Range profile with different Doppler frequency for FMCW and the phase lag compensated PC-FMCW waveforms with $N_c = 1024$. (a) FMCW. (b) BPSK. (c) Gaussian. (d) GMSK. The ridge is inclined in all cases but seems narrow due to zooming out the x-axis.

properties, we assume a noise-free scenario in the numerical simulations.

A. Sensing

The sensing performance of the phase lag compensated waveforms are assessed by using the investigated processing method and compared with FMCW. After proper decoding, the code term is removed, and the beat signal is recovered similar to the dechirped signal of traditional FMCW as explained in Section IV.

To investigate the Doppler tolerance of the waveforms and proposed receiver strategy, we simulate the received signal after dechirping (5) as a function of Doppler frequency shift and plot the outcome of the introduced processing approach in a form similar to the ambiguity function in Fig. 11. The presented plots show the behavior of FMCW and three phase lag compensated PC-FMCW with $N_c = 1024$ after processing. It can be seen that the inclined ridge associated with the chirped waveform ambiguity function is present

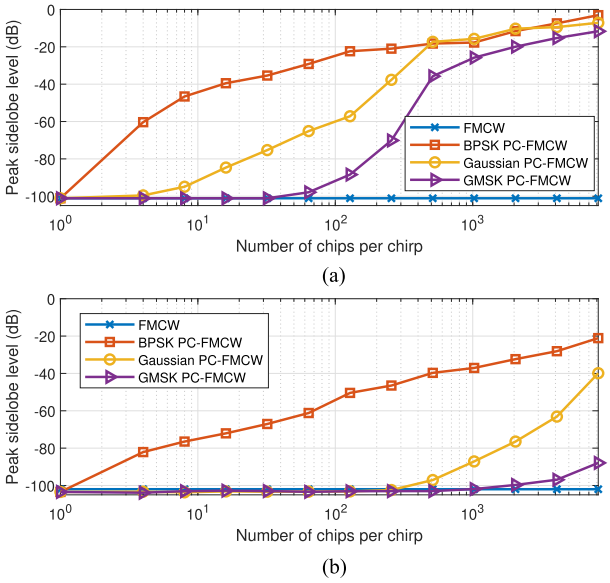

Fig. 12. PSL of the investigated waveforms at normalized target range $R/R_{\max} = 0.4$ versus the number of chips per chirp. (a) No phase lag compensation. (b) With phase lag compensation.

and the same in Fig. 11(a)– (d). Thus, all considered waveforms have the Doppler tolerance of FMCW and exhibit the range-Doppler coupling, determined by the slope of the carrier chirp. Note that the x-axis is zoomed out to highlight the sidelobe differences between waveforms, and hence, the inclined ridge seems like a narrow line. In the vicinity of the main lobe, they all have an identical response, determined by 100 dB Chebyshev window, applied to the signals before range FFT. The sidelobes of three phase lag compensated PC-FMCW raises with the Doppler frequency shift; among them, the range profile degradation is minimal for GMSK.

The bandwidth of the chip B_c raises as the number of chips per chirp N_c increases. Consequently, the bandwidth of the chip becomes comparable to ADC sampling frequency, and the sidelobe level increases with the filtering of the spectrum. However, the spectrum widening of the coded beat signal is different for the three phase lag compensated PC-FMCW, as explained in Section III. Therefore, they provide different peak sidelobe level (PSL). The beat signal PSL is defined by the maximum amplitude of the signal spectrum outside of the main lobe (first nulls) and can be written as

$$\mathrm{PSL} = \max_{f \in \mathcal{L}} \left|\hat{Z}_{\mathrm{d}}(f)\right| \qquad \mathcal{L} = (-\infty, -f_l) \cup (f_r, \infty) \quad (48)$$

where f_l and f_r denote the frequency corresponding to the left and right parts of the first null, respectively, and $\mathcal{L}$ denotes the frequency interval.

Next, we investigate the zero-Doppler cuts of waveforms and compare their respective peak sidelobe levels. PSL of the investigated waveform at normalized target range $R/R_{\max} = 0.4$ as a function of the number of chips per chirp is demonstrated in Fig. 12 where the maximum range $R_{\max} = \frac{c f_{b_{\max}}}{2k}$ and the maximum beat signal is determined as $f_{b_{\max}} = f_s/2$. To highlight the benefits of performing

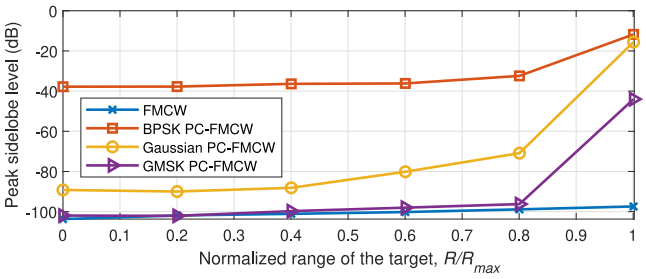

Fig. 13. PSL of the investigated waveforms (with phase lag compensation) with $N_c = 1024$ versus the normalized range of the target with respect to the maximum range.

phase lag compensation, we also demonstrate the sensing performance of investigated waveforms without performing phase lag compensation in Fig. 12(a). It can be seen that applying phase lag compensation improves the PSL of three PC-FMCW waveforms, see Fig. 12(b). Still, the PSL of BPSK PC-FMCW rapidly increases as the number of chips per chirp raises. On the other hand, we observe that the PSL of phase lag compensated GMSK PC-FMCW enhanced substantially, especially for long codes. Particularly, the PSL of GMSK PC-FMCW with $N_c = 1024$ improved from -25 to -100 dB by using phase lag compensation. Consequently, GMSK PC-FMCW can provide PSL similar to FMCW up to $N_c = 1024$. In addition, we illustrated the PSL of phase lag compensated waveforms with $N_c = 1024$ as a function of the normalized target range in Fig. 13. Note that the spectral widening and filtering of the spectrum become crucial for PC-FMCW as the target approaches the maximum range. GMSK PC-FMCW has favorable sensing performance among phase lag compensated waveforms and provides lower PSL.

B. Peak to Average Power Ratio

The quadratic phase lag compensation is applied to the spectrum of the transmitted code to eliminate the dispersion effect of the group delay filter. This quadratic phase lag compensation filter can be represented as

$$H_{\text{lag}}(f) = e^{-j\frac{\pi f^2}{k}} \tag{49}$$

and the phase lag compensated code term in the time domain can be written as

$$\hat{s}(t) = s(t) \otimes h_{\text{lag}}(t). \tag{50}$$

To analyze the effect of quadratic phase lag compensation on a phase-coded signal, let $\xi = j\frac{\pi}{k}$, then the quadratic phase lag compensation filter in the time domain can be written as

$$\begin{aligned} h_{\text{lag}}(t) &= \int_{-\infty}^{\infty} e^{-\xi f^2} e^{j2\pi ft}\, df \\ &= e^{-\frac{\pi^2 t^2}{\xi}} \int_{-\infty}^{\infty} e^{-\left(\sqrt{\xi} f - j\frac{\pi t}{\sqrt{\xi}}\right)^2} df \\ &= \sqrt{\frac{k}{j}} e^{-\pi \frac{kt^2}{j}}. \end{aligned} \tag{51}$$

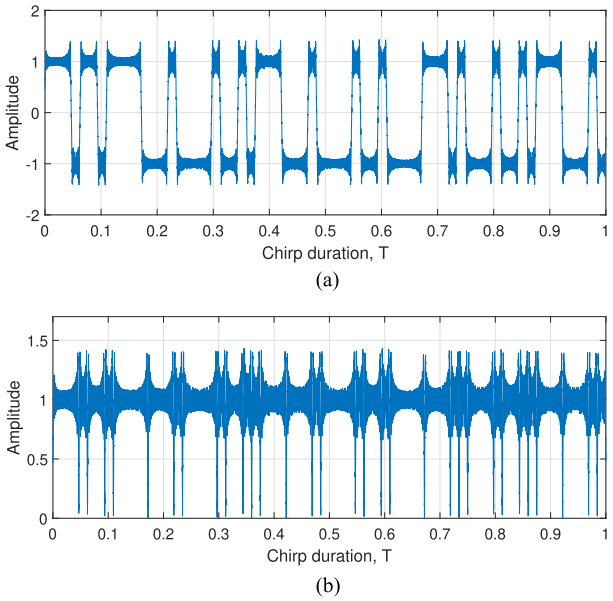

Fig. 14. Time-varying amplitude due to phase lag compensation. (a) BPSK code $N_c = 64$. (b) Absolute value of the transmitted BPSK PC-FMCW.

Subsequently, the result of the convolution for the BPSK code sequence becomes

$$\begin{aligned} \hat{s}(t) &= c(t) \otimes h_{\text{lag}}(t) \\ &= \frac{1}{T}\frac{1}{T_c}\frac{1}{2} \sum_{n=1}^{N_c} e^{j(\phi_{n+1}-\phi_n)} \text{erf}\left(\sqrt{\frac{\pi k}{j}}\,(t - nT_c)\right). \end{aligned} \tag{52}$$

The proof is given in Appendix B. The amplitude of the phase lag compensated BPSK code is shown in Fig. 14(a). The quadratic phase lag compensation applies different time delays to each frequency component of the transmitted phase code. During phase changes, the phase-coded signal has a wide spectrum, and shifting the frequency components nonlinearly creates ripples in the time domain signal, see Fig. 14(a). Moreover, the time interval between phase changes becomes shorter for a long code sequence, and ripples in the time domain are collectively summed up as the adjacent phase shifts interfering with each other. Therefore, the amplitude of the transmitted waveform is not constant anymore, see Fig. 14(b).

The time-varying amplitude initiated by the phase lag compensation leads to a high peak-to-average power ratio (PAPR). The PAPR of the signal can be represented as

$$\text{PAPR} = \frac{\max|x_{\text{T}}(t)|^2}{\lim_{T\to\infty} \frac{1}{2T} \int_{-T}^{T} |x_{\text{T}}(t)|^2\, dt}. \tag{53}$$

The PAPR of the investigated waveforms is compared as a function of N_c in Fig. 15. It can be seen that the PAPR of the three PC-FMCW without phase lag compensation are constant and equal to 1. The PAPR increases for all three phase lag compensated PC-FMCW as N_c raises. However, the effect of the phase lag compensation and the resulting amplitude variation decrease as the phase transition becomes smoother. Note that the differences of PAPR between

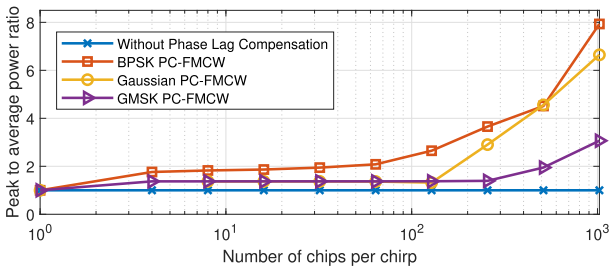

Fig. 15. Comparison of PAPR versus number of chips per chirp for phase lag compensated PC-FMCW waveforms.

BPSK, Gaussian, and GMSK are comparable up to $N_c = 64$; thereafter, PAPR varies notably. For long code sequences, GMSK PC-FMCW provides the lowest PAPR while BPSK PC-FMCW has the highest PAPR since the abrupt phase changes on the BPSK coding are affected more by the frequency-dependent shifts.

C. Mutual Orthogonality

The coding spreads the power of the signals in the beat frequency domain. As each transmitted PC-FMCW uses its phase-coded signal, only the correct signal passes through the received signal, which is matched to this code. The signals with other code sequences are not matched to this code, leading to the spread of the power over range. The theoretical limits of the suppression are equal to the spreading factor and can be written as [10]

$$SP \equiv 10\log\left(\frac{BT}{BT_c}\right) = 10\log_{10}(N_c). \tag{54}$$

Assume the first radar (victim) transmits PC-FMCW with the phase lag compensated code $\hat{s}_1(t)$ to detect a target. The received signal reflected from the target with complex coefficient α_1 can be written as

$$x_{\mathrm{R}_1}(t) = \alpha_1 \hat{s}_1(t-\tau_1)e^{-j\left(2\pi f_c(t-\tau_1)+\pi k(t-\tau_1)^2\right)}. \tag{55}$$

To illustrate the mutual orthogonality assessment, consider the worst-case scenario when a second radar is perfectly synchronized with the first radar and transmits PC-FMCW with the phase lag compensated code $\hat{s}_2(t)$. The signal transmitted from the second radar is delayed in time and captured by the first radar with complex coefficient α_2 as

$$x_{\mathrm{R}_2}(t) = \alpha_2 \hat{s}_2(t-\tau_2)e^{-j\left(2\pi f_c(t-\tau_2)+\pi k(t-\tau_2)^2\right)} \tag{56}$$

where τ_2 is the round trip delay between the first and second radars. Subsequently, the total received signal on the first radar is the combination of received signals and can be written as

$$x_{\mathrm{R}}(t) = x_{\mathrm{R}_1}(t) + x_{\mathrm{R}_2}(t). \tag{57}$$

The total received signal is mixed and dechirped with the uncoded transmit signal of the first radar. The mixer output gives the summation of two coded beat signals. Subsequently, the group delay filter is applied to the mixer output and aligns coded beat signals at the maximum delay, as discussed in Section IV. The output of the group delay filter can be represented as

$$g_{\mathrm{o}}(t) = \alpha_1 s_1(t-\tau_{\max})e^{j(2\pi k\tau_1 t)} + \alpha_2 s_2(t-\tau_{\max})e^{j(2\pi k\tau_2 t)}. \tag{58}$$

During decoding, the group delay filter output is decoded with the complex conjugate of the first code shifted to the maximum delay $s_1(t-\tau_{\max})$. After decoding, the beat signal reflected from the target is obtained similar to the dechirped signal of conventional FMCW, while the beat signal initiated by the second radar remains coded as

$$\begin{aligned} d_{\mathrm{o}}(t) &= d_1(t) + d_2(t) \\ &= \alpha_1 e^{j(2\pi k\tau_1 t)} + \alpha_2 s_1^*(t-\tau_{\max})s_2(t-\tau_{\max})e^{j(2\pi k\tau_2 t)} \end{aligned} \tag{59}$$

where $d_1(t)$ and $d_2(t)$ are the decoded signals. Subsequently, we investigate the cross-isolation between two beat signals in the spectrum of the decoded signal output. The cross-isolation can be defined as

$$\text{cross-isolation} = \frac{\max_{f\in\forall}|D_1(f)|}{\max_{f\in\forall}|D_2(f)|} \tag{60}$$

where $D_1(f)$ and $D_2(f)$ are the spectrum of decoded signals associated with $d_1(t)$ and $d_2(t)$, respectively.

In Fig. 16, we compare the cross-isolation between the two beat signals associated with PC-FMCW waveforms with different random code sequences. We consider the number of chips per chirp $N_c = 1024$ and the number of chirp pulses $N_p = 512$. It is shown in Fig. 16 that the second radar causes a beat signal according to $f_{b_2} = k\tau_2$, which can be seen as a ghost target for a perfectly synchronized case (which is very difficult to generate in a real-life scenario and is just used for the proof of the mutual orthogonality concept), and it cannot be distinguished from the target in the traditional FMCW, see Fig. 16(a). However, in the phase-coded FMCW cases, the beat signal initiated by the second radar f_{b_2} remains coded, and thus, its power is spread over both fast-time and slow-time. This cross-isolation between two beat signals associated with BPSK PC-FMCW, Gaussian PC-FMCW, and GMSK PC-FMCW is given in Fig. 16(b)–(d), respectively. The theoretical upper boundary limit regarding the suppression of the beat signal f_{b_2} is $10\log_{10}(512) + 10\log_{10}(1024) = 57$ dB for a perfectly orthogonal code (combined with the suppression in both slow-time and fast-time). However, the three phase lag compensated PC-FMCW are not perfectly orthogonal after applying the phase lag compensation and filtering. Their resulting suppression behaviors in the fast-time are different according to their phase modulation type, as shown in Fig. 16. In particular, Gaussian PC-FMCW has the local peaks between phase-coded signals, and it gives the worst suppression performance. BPSK PC-FMCW spreads the power of f_{b_2} to all range cells as the spectrum of BPSK has a significant spectrum broadening of the beat signal. GMSK PC-FMCW spreads the power of the f_{b_2} as a Gaussian shape (triangular in dB scale) over the range cells defined by the 3-dB bandwidth of the Gaussian filter (smoother bandwidth) B_s. Consequently, GMSK PC-FMCW has a narrower spreading characteristic than BPSK, which might

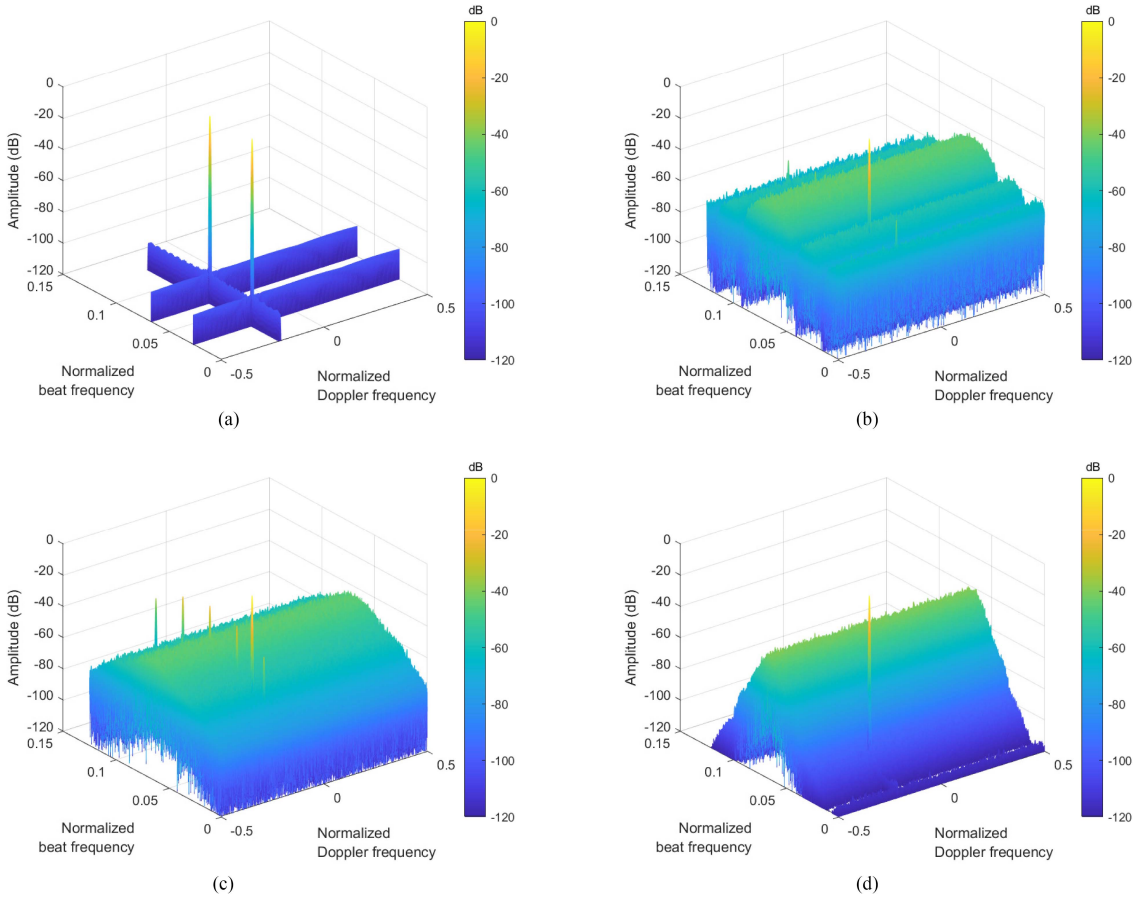

Fig. 16. Comparison of cross-isolation between two beat signals associated with three phase lag compensated PC-FMCW waveforms with different random codes. (a) FMCW (no code). (b) BPSK. (c) Gaussian. (d) GMSK.

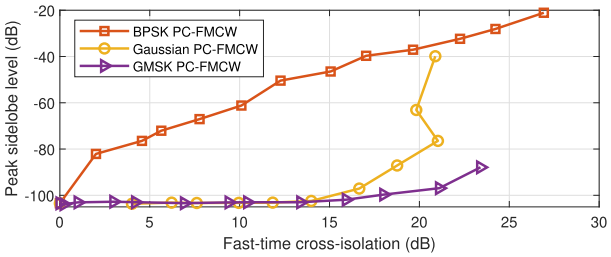

Fig. 17. Comparison of PSL versus cross-isolation in fast-time for phase lag compensated PC-FMCW waveforms.

Fig. 18. Illustration of the stationary target.

help to avoid masking of targets with weak radar cross section (RCS) outside of main lobe. Moreover, it can be seen in Fig. 17 that GMSK PC-FMCW can provide high cross-isolation while achieving low PSL. These facts favor the usage of GMSK PC-FMCW over BPSK PC-FMCW.

VI. EXPERIMENTS

This section demonstrates the experimental results related to the sensing and cross-isolation performance of the phase lag compensated PC-FMCW waveforms. The experimental investigation of the waveforms has been done using PARSAX radar [31]. We use the proposed transceiver structure for each PC-FMCW, and we apply the traditional dechirping transceiver structure for the FMCW waveform, which is used as a benchmark. We use random code sequences with $N_C = 1024$ for the three phase lag compensated PC-FMCW and choose the system parameters as given in Table I. To emphasize the advantage of GMSK, we choose ADC sampling frequency as $f_{\text{ADC}} = 2$ MHz so that the code bandwidth becomes comparable to ADC sampling. Moreover, we applied Chebyshev windowing with 80 dB suppression and compared it with a rectangle windowing case to highlight the sensing performance of the waveforms. In addition, we normalized all the range profiles by the maximum of the range profile.

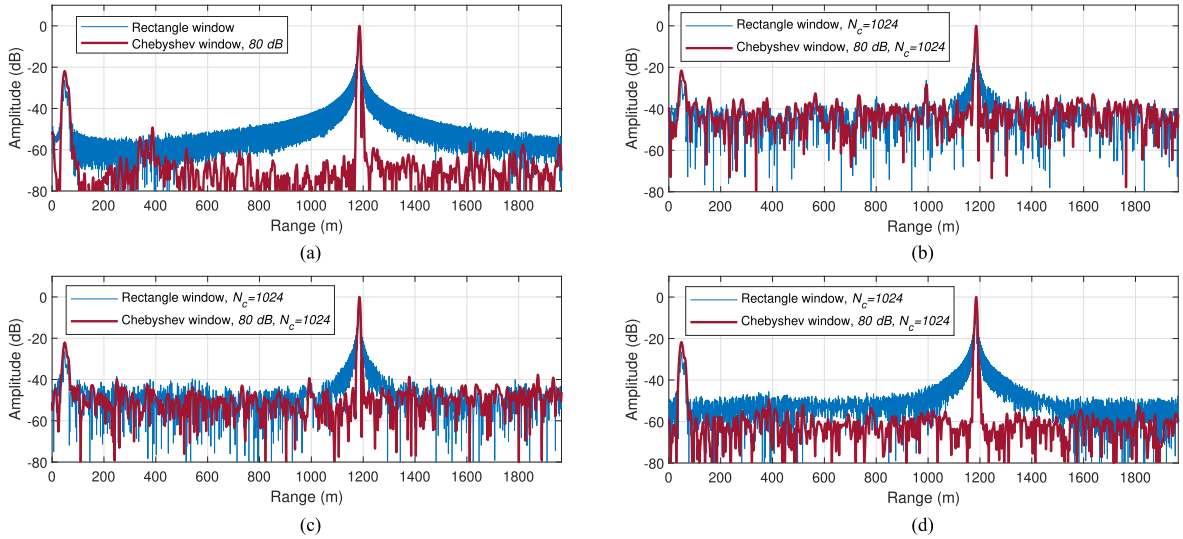

Fig. 19. Stationary target range profiles for phase lag compensated PC-FMCW waveforms. (a) FMCW. (b) BPSK. (c) Gaussian. (d) GMSK.

TABLE I
System Parameters

Chirp bandwidth	B	40 MHz
Chirp duration	T	1 ms
Intermediate frequency	f_{IF}	125 MHz
IF sampling frequency	f_s	400 MHz
Carrier frequency	f_c	3.315 GHz
ADC sampling frequency	f_{ADC}	2 MHz
Number of chips	N_c	1024
Chip duration	T_c	0.97μ s
Chip bandwidth	B_c	1.024 MHz
Smoother bandwidth	B_s	2.048 MHz

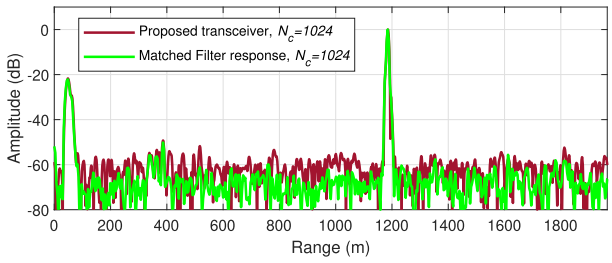

Fig. 20. Range profile for phase lag compensated GMSK PC-FMCW in the case of the proposed transceiver and matched filter.

Fig. 21. Illustration of the moving target.

A. Sensing Performance of One Waveform

In this section, we transmit only one waveform at a time to validate the sensing performance of the waveforms. The resulting waveforms are performed in the real scenario to detect both stationary and moving targets. Note that the experimental environment is dynamic for the moving target experiment. To detect the same car and compare the sensing performance of the waveforms, we transmit four waveforms sequentially with 128 chirp pulses in each waveform.

1) *Stationary Target Experiment:* For the stationary target experiment, we look at the chimney located at 1185 m away from the radar, as shown in Fig. 18. The range profiles of the four different waveforms are demonstrated in Fig. 19. At the chimney location, the noise-clutter level of the range profile is around ~ -60 dB for FMCW, and it provide ~ 60 dB dynamic range after applying Chebyshev windowing. It can be seen that BPSK and Gaussian have increased sidelobes and provides ~ 30 and ~ 40 dB dynamic ranges, respectively. This is due to the fact that BPSK and Gaussian have substantial broadening in the beat frequency and the coded beat signals have a wide spectrum. As a result, the sensing performance of BPSK and Gaussian suffers from limited ADC sampling. On the other hand, widening of the coded beat signal spectrum is reduced by using GMSK, as explained in Section III. Thus, GMSK is expected to provide better sensing performance while the code bandwidth becomes comparable to ADC sampling. We observe this behavior as GMSK provides the best and closest performance to FMCW by providing ~ 60 dB dynamic range in the vicinity of the chimney. In addition, we demonstrate the range profile of GMSK PC-FMCW by using matched filter receiving strategy and compared it with the response of the proposed transceiver structure in Fig. 20. It can be seen that the proposed transceiver structure gives a very similar result to the matched filter response for GMSK PC-FMCW.

2) *Moving Target Experiment:* The Doppler tolerance of the investigated waveforms is validated by the moving target experiment where we observe the road and detect a

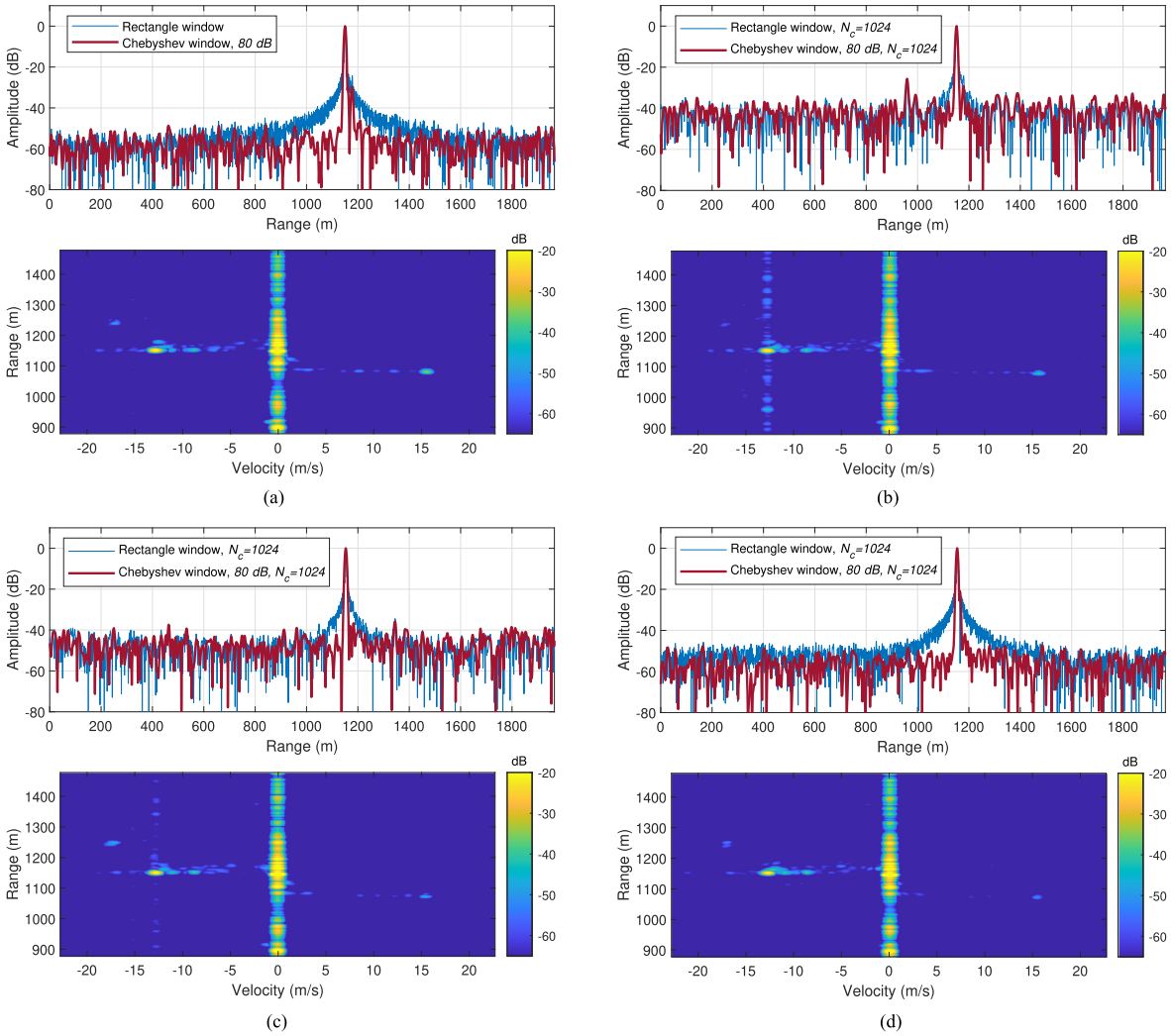

Fig. 22. Moving target range and range-Doppler profiles for phase lag compensated PC-FMCW waveforms. (a) FMCW. (b) BPSK. (c) Gaussian. (d) GMSK.

moving car located at 1150 m with a radial velocity $\sim$ 13 m/s, as illustrated in Fig. 21. We use $N_c = 1024$ for the three phase lag compensated PC-FMCW. The range-Doppler profiles of the waveforms are demonstrated in Fig. 22 where the peak location of the target is obtained at 1150 m for each waveform. The noise level of the range profile is around ~ -55 dB for FMCW, and it has $\sim$ 55 dB dynamic range after windowing, see Fig. 22(a). Similar to the stationary target scenario, GMSK provides the best sensing performance between three phase lag compensated PC-FMCW. In particular, the range profile of BPSK PC-FMCW has increased sidelobe level due to limited ADC sampling, and it provides a dynamic range around $\sim$ 30 dB, see Fig. 22(b), whereas the sidelobe level of Gaussian PC-FMCW provides $\sim$ 40 dB dynamic range, see Fig. 22(c). However, GMSK PC-FMCW provides $\sim$ 55 dB dynamic range, and it has a range profile very similar to FMCW, as shown in Fig. 22(d). Consequently, GMSK PC-FMCW can provide similar sensing performance that is offered by FMCW, and it can also ensure the ability to distinguish different signals due to coding, as discussed in Section V-C.

B. Cross-Isolation Performance Between two Waveforms

In this section, we transmit two same types of waveforms simultaneously to validate the cross-isolation performance of the waveforms. For the proof of the mutual orthogonality concept and to mimic the worst-case scenario, as explained in Section V-C, we apply linear time delay to the second waveform so that it has a range offset compared with the first waveform that corresponds to 480 m. For each PC-FMCW, the first waveform uses phase lag compensated random code $\hat{s}_1(t)$ with $N_c = 1024$, and the second waveform uses phase lag compensated random code $\hat{s}_2(t)$ with $N_c = 1024$. Moreover, we use 32 chirp pulses, and each PC-FMCW chirp pulses use different random code sequences. Consequently, combined with the suppression in both slow-time and fast-time, the theoretical upper boundary limit of cross-isolation is $10\log_{10}(32) +$

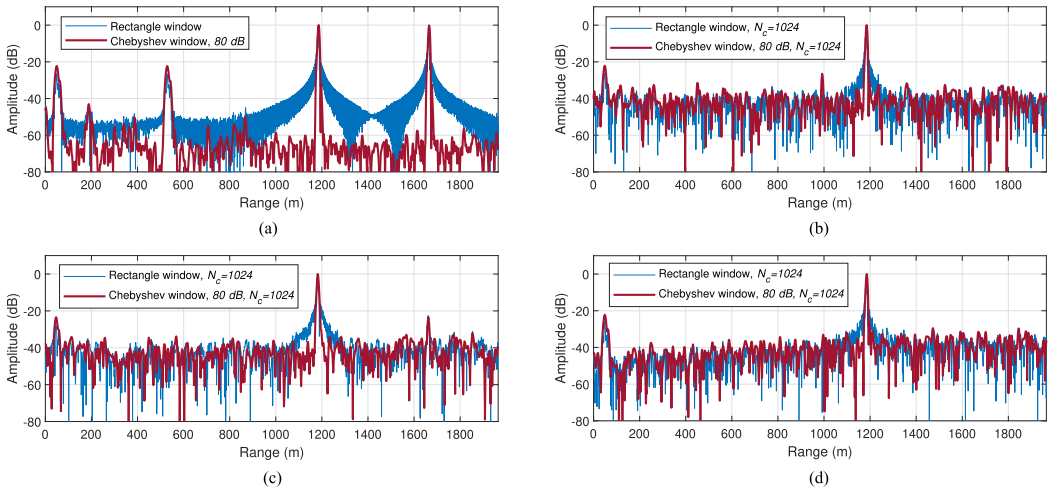

Fig. 23. Cross-isolation experiment for a stationary target. Range profiles for phase lag compensated PC-FMCW waveforms. (a) FMCW. (b) BPSK. (c) Gaussian. (d) GMSK.

$10\log_{10}(1024) = 45$ dB for a perfectly orthogonal code. However, the cross-isolation performance is expected to be degraded due to the loss of orthogonality between codes after applying the phase lag compensation and filtering. The resulting two waveforms are transmitted together and performed in the real scenario to detect the chimney located at 1185 m away from the radar. Subsequently, the received signal for each PC-FMCW is processed with the proposed transceiver structure and decoded with the reference code $s_1(t)$.

The range profiles of the four different waveforms are demonstrated in Fig. 23. It can be seen that the second FMCW waveform leads to a beat signal that causes ghost targets at 530 and 1665 m in addition to real targets at 50 and 1185 m. Since there is no mutual orthogonality between two FMCW waveforms, the second waveform cannot be distinguished from the first waveform in the traditional FMCW radar. By using PC-FMCW waveforms, only the beat signal associated with the first waveform is decoded with $s_1(t)$ and the beat signal initiated by the second waveform is spread over both fast-time and slow-time as it remains coded. Consequently, the ghost targets created by the second waveform are suppressed using PC-FMCW. Among three phase lag compensated PC-FMCW, GMSK provides the best dynamic range. Particularly, Gaussian PC-FMCW provides weak suppression performance, and the ghost target still appears with ~ -22 dB power. BPSK PC-FMCW suppresses the ghost target power around ~ 34 dB but only provides ~ 26 dB dynamic range as it suffers from limited ADC sampling. On the other hand, GMSK suppresses the ghost target's power and provides ~ 40 dB dynamic range in the vicinity of the chimney. Thus, experimental results verify the advantages of GMSK PC-FMCW over BPSK PC-FMCW and Gaussian PC-FMCW.

VII. CONCLUSION

The smoothing of the phase-coded frequency modulated continuous waveform has been introduced as an efficient tool to enhance the coexistence of multiple radars within the same spectrum. The impact of the spectrum widening due to the abrupt phase changes of BPSK is investigated, and the Gaussian filter is proposed to smooth the phase transition of PC-FMCW. We have suggested a receiving strategy with a low sampling requirement and analyzed the group delay filter effect on the coded beat signals. In addition, the phase lag compensation is performed on the transmitted phase-coded signal to eliminate the undesired effect of the group delay filter and recover the beat signals properly after the decoding.

The properties of the investigated waveforms for the first time are analyzed theoretically and verified experimentally. It is shown that the PSL, PAPR, and the cross-isolation between signals increase as the bandwidth of the code raises for the three phase lag compensated PC-FMCW. The simulations and the experimental results demonstrate that the phase lag compensated GMSK PC-FMCW can provide sensing performance similar to that of uncoded FMCW. At the same time, it can provide high mutual orthogonality that can be used to improve cross-isolation between multiple radars.

APPENDIX A
DERIVATIVES OF DIFFERENT TYPES OF PHASE CODE

In this proof, we demonstrate the taking derivative of the different types of phase code with respect to time. Recall that the rectangle function can be written as

$$\text{rect}\left(\frac{t-x}{y}\right) = u\left(t-x+\frac{y}{2}\right) - u\left(t-x-\frac{y}{2}\right) \quad (61)$$

where u is a unit step function. Similarly, the code term can be written as

$$\phi_n \text{rect}\left(\frac{t-\left(n-\frac{1}{2}\right)T_c}{T_c}\right) = \phi_n u\left(t-\left(n-\frac{1}{2}\right)T_c+\frac{T_c}{2}\right) - \phi_n u\left(t-\left(n-\frac{1}{2}\right)T_c-\frac{T_c}{2}\right) \quad (62)$$

and

$$\phi_{n+1}\text{rect}\left(\frac{t-\left(n+\frac{1}{2}\right)T_c}{T_c}\right) = \phi_{n+1}u\left(t-\left(n+\frac{1}{2}\right)T_c+\frac{T_c}{2}\right) - \phi_{n+1}u\left(t-\left(n+\frac{1}{2}\right)T_c-\frac{T_c}{2}\right) \quad (63)$$

for the nth and $(n+1)$th elements, respectively. Note that the $\phi_n \in \{0, \pi\}$ denotes the phase corresponding to the n^{th} bit of the N_c bits sequence. To take the summation of unit step functions, we have to consider a junction point in which the adjacent elements are linked. Thus, the relevant junction point includes the right part of the nth and left part of the $(n+1)$th elements, and the phase of the BPSK code can be represented as

$$\phi_{\text{bpsk}}(t) = \sum_{n=1}^{N_c}(\phi_{n+1}-\phi_n)\,u(t-nT_c) \quad (64)$$

where the amplitude of the unit step function varies between π and $-\pi$ depending on the value $(\phi_{n+1}-\phi_n)$, and the summation of the unit step functions gives the phase of the BPSK code sequence $\phi_{\text{bpsk}}(t) \in \{0, \pi\}$. In the following sections, we derive the instantaneous frequency of the different types of phase code.

A. BPSK

Taking the derivative of the $\phi_{\text{bpsk}}(t)$ gives

$$\frac{1}{2\pi}\frac{d}{dt}\phi_{\text{bpsk}}(t) = \frac{1}{2\pi}\sum_{n=1}^{N_c}(\phi_{n+1}-\phi_n)\,\delta(t-nT_c) \quad (65)$$

where δ is the Dirac delta function. Same result can be seen in [25].

B. Gaussian

The convolution of the unit step function with filter $h_0(t) = e^{-t^2}$, where $t \geq 0$ and can be represented as

$$u(t)\otimes h_0(t) = \int_{-\infty}^{\infty} h_0(\tau)u(t-\tau)d\tau = \int_0^t h_0(\tau)d\tau = \int_0^t e^{-\tau^2}d\tau = \frac{\sqrt{\pi}}{2}\text{erf}(t) \quad (66)$$

where erf(t) represents the error function as

$$\text{erf(t)} = \frac{2}{\sqrt{\pi}}\int_0^{\text{t}} \text{e}^{-\text{t}^2}\,\text{dt}\,. \quad (67)$$

Subsequently, the convolution of the unit step function and the Gaussian filter $h(t) = \frac{\eta}{\sqrt{\pi}}e^{-\eta^2t^2}$ can be written as

$$u(t)\otimes h(t) = \int_0^t h(\tau)d\tau = \int_0^t \frac{\eta}{\sqrt{\pi}}e^{-\eta^2\tau^2}d\tau. \quad (68)$$

Replacing $\gamma = \eta\tau$ and $d\gamma = \eta d\tau$, the equation becomes

$$u(t)\otimes h(t) = \frac{1}{\sqrt{\pi}}\int_0^{\eta t} e^{-\gamma^2}d\gamma = \frac{1}{2}\text{erf}(\eta t). \quad (69)$$

Consequently, the phase of the Gaussian binary code can be written as

$$\phi_{\text{gauss}}(t) = \phi_{\text{bpsk}}(t)\otimes h(t) = \frac{1}{2}\sum_{n=1}^{N_c}(\phi_{n+1}-\phi_n)\,\text{erf}\,(\eta(t-nT_c))\,. \quad (70)$$

The derivative of the error function can be obtained as

$$\frac{d}{dt}\,(\text{erf(t)}) = \frac{2}{\sqrt{\pi}}e^{-t^2}. \quad (71)$$

Subsequently, taking the derivative of (70) with respect to time gives

$$\frac{1}{2\pi}\frac{d}{dt}\phi_{\text{gauss}}(t) = \frac{\eta}{2\pi\sqrt{\pi}}\sum_{n=1}^{N_c}(\phi_{n+1}-\phi_n)e^{-\eta^2(t-nT_c)^2}. \quad (72)$$

C. GMSK

The phase of the GMSK can be represented as

$$\phi_{\text{gmsk}}(t) = \int_{-\infty}^{\infty}\phi_{\text{gauss}}(t)dt = \int_{-\infty}^{\infty}(\phi_{\text{bpsk}}(t)\otimes h(t))dt. \quad (73)$$

Taking the derivative of the $\phi_{\text{gmsk}}(t)$ gives

$$\frac{1}{2\pi}\frac{d}{dt}\phi_{\text{gmsk}}(t) = \frac{1}{2\pi}\phi_{\text{gauss}}(t) = \frac{1}{4\pi}\sum_{n=1}^{N_c}(\phi_{n+1}-\phi_n)\,\text{erf}\,(\eta(t-nT_c))\,. \quad (74)$$

APPENDIX B
CONVOLUTION WITH PHASE LAG COMPENSATION

In this proof, we demonstrate the result of the convolution with phase lag compensation. Let $\beta = \sqrt{\frac{\pi k}{j}}$, then (51) becomes

$$h_{\text{lag}}(t) = \frac{\beta}{\sqrt{\pi}}e^{-\beta^2t^2}. \quad (75)$$

Following the steps between (66) and (69) given in Appendix A, and replacing $\eta = \beta$, the convolution of the unit step function and phase lag compensation filter can be found as

$$u(t)\otimes h_{\text{lag}}(t) = \frac{1}{2}\text{erf}\left(\sqrt{\frac{\pi k}{j}}t\right). \quad (76)$$

Subsequently, the result of the convolution for the BPSK code sequence becomes

$$\begin{aligned}\hat{\mathrm{s}}(t) &= c(t) \otimes h_{\mathrm{lag}}(t) \\ &= \frac{1}{T}\frac{1}{T_c}\frac{1}{2}\sum_{n=1}^{N_c} e^{j(\phi_{n+1}-\phi_n)}\mathrm{erf}\left(\sqrt{\frac{\pi k}{j}}\,(t-nT_c)\right). \quad (77)\end{aligned}$$

APPENDIX C
GROUP DELAY FILTER PHASE RESPONSE

In this proof, we demonstrate the relationship between phase response and group delay. To ease of mathematical manipulations, let

$$\begin{aligned} d &= \theta(f_b) - f_b\,\frac{d\theta(f)}{df}\Big|_{f=f_b} \\ p &= \frac{d\theta(f)}{df}\Big|_{f=f_b} \\ \varphi(f) &= \sum_{m=2}^{\infty}\frac{1}{m!}\frac{d^m\theta(f)}{df^m}\Big|_{f=f_b}(f-f_b)^m. \quad (78)\end{aligned}$$

Subsequently, multiplying the group delay filter with the mixer output in frequency domain gives

$$\begin{aligned} Z_{\mathrm{o}}(f) &= X_{\mathrm{M}}(f)H_{\mathrm{g}}(f) \\ &= S(f-f_b)e^{-j\left(\frac{2\pi f_b}{k}(f-f_b)\right)}e^{j(d+pf)}e^{j\varphi(f)}. \quad (79)\end{aligned}$$

Note that $\varphi(f)$ term is small compared with first two terms due to the Taylor series expansion. Taking the inverse Fourier transform of the group delay filter output gives

$$\begin{aligned} z_{\mathrm{o}}(t) &= \mathcal{F}^{-1}\left\{S(f-f_b)e^{-j\left(\frac{2\pi f_b}{k}(f-f_b)\right)}e^{j(d+pf)}\right\} \\ &\quad \otimes \mathcal{F}^{-1}\left\{e^{j\varphi(f)}\right\} \\ &= z_1(t)\otimes z_2(t). \quad (80)\end{aligned}$$

The resulting signal can be considered as the convolution of two signal as $z_{\mathrm{o}}(t) = z_1(t)\otimes z_2(t)$. The right part of the convolution $z_2(t) = \mathcal{F}^{-1}\{e^{j\varphi(f)}\}$ comes from the higher order terms in Taylor series expansion and leads to so-called dispersion effect. The left part of the convolution $z_1(t)$ causes the group delay that we are interested in and can be obtained as

$$\begin{aligned} z_1(t) &= \mathcal{F}^{-1}\left\{S(f-f_b)e^{-j\left(\frac{2\pi f_b}{k}(f-f_b)\right)}e^{j(d+pf)}\right\} \\ &= \int_{-\infty}^{\infty} S(f-f_b)e^{-j\left(\frac{2\pi f_b}{k}(f-f_b)\right)}e^{j(d+pf+2\pi ft)}\,df \\ &= \int_{-\infty}^{\infty} S(f_1)e^{-j\left(\frac{2\pi f_b}{k}(f_1)\right)}e^{j(d+p(f_1+f_b)+2\pi(f_1+f_b)t)}\,df_1 \\ &= \int_{-\infty}^{\infty} S(f_1)e^{j\left(2\pi f_1(t-\frac{f_b}{k}+\frac{p}{2\pi})\right)}\,df_1\;e^{j(d+f_b(2\pi t+p))} \\ &= s\left(t-\frac{f_b}{k}+\frac{p}{2\pi}\right)e^{j(d+f_b(2\pi t+p))} \\ &= s\left(t-\tau_0+\frac{1}{2\pi}\frac{d\theta(f)}{df}\Big|_{f=f_b}\right)e^{j(2\pi f_b t)}e^{j(\theta(f_b))} \\ &= s\left(t-\tau_0-\tau_g(f)\right)e^{j(2\pi f_b t)}e^{j(\theta(f_b))}. \quad (81)\end{aligned}$$

As a result, the filter leads to the group delay $\tau_g(f)$, which shifts the envelope of the signal.

ACKNOWLEDGMENT

The authors would like to thank Fred van der Zwan and Yun Lu for their support during the experiments and Tworit Dash for his helpful suggestions. The authors would also like to thank the anonymous reviewers for their constructive comments that improved the quality of this article significantly.

REFERENCES

[1] G. M. Brooker, "Mutual interference of millimeter-wave radar systems," *IEEE Trans. Electromagn. Compat.*, vol. 49, no. 1, pp. 170–181, Feb. 2007.

[2] S. D. Blunt and E. L. Mokole, "Overview of radar waveform diversity," *IEEE Aerosp. Electron. Syst. Mag.*, vol. 31, no. 11, pp. 2–42, Nov. 2016.

[3] F. Liu, C. Masouros, A. Petropulu, H. Griffiths, and L. Hanzo, "Joint radar and communication design: Applications, state-of-the-art, and the road ahead," *IEEE Trans. Commun.*, vol. 68, no. 6, pp. 3834–3862, Jun. 2020.

[4] C. Aydogdu et al., "Radar interference mitigation for automated driving: Exploring proactive strategies," *IEEE Signal Process. Mag.*, vol. 37, no. 4, pp. 72–84, Jul. 2020.

[5] J. Wang, M. Ding, and A. Yarovoy, "Matrix-pencil approach-based interference mitigation for FMCW radar systems," *IEEE Trans. Microw. Theory Techn.*, vol. 69, no. 11, pp. 5099–5115, Nov. 2021.

[6] S. Neemat, O. Krasnov, and A. Yarovoy, "An interference mitigation technique for FMCW radar using beat-frequencies interpolation in the STFT domain," *IEEE Trans. Microw. Theory Techn.*, vol. 67, no. 3, pp. 1207–1220, Mar. 2019.

[7] L. L. Tovar Torres, M. Steiner, and C. Waldschmidt, "Channel influence for the analysis of interferences between automotive radars," in *Proc. 17th Eur. Radar Conf.*, 2021, pp. 266–269.

[8] J. Overdevest, F. Laghezza, F. Jansen, and A. Filippi, "Radar waveform coexistence: Interference comparison on multiple-frame basis," in *Proc. 17th Eur. Radar Conf.*, 2021, pp. 168–171.

[9] I. Bilik, O. Longman, S. Villeval, and J. Tabrikian, "The rise of radar for autonomous vehicles: Signal processing solutions and future research directions," *IEEE Signal Process. Mag.*, vol. 36, no. 5, pp. 20–31, Sep. 2019.

[10] M. Jankiraman, *FMCW Radar Design*. Norwood, MA, USA: Artech House, 2018.

[11] J. Bechter, K. Eid, F. Roos, and C. Waldschmidt, "Digital beamforming to mitigate automotive radar interference," in *Proc. IEEE MTT-S Int. Conf. Microw. Intell. Mobility*, 2016, pp. 1–4.

[12] M. Umehira, Y. Makino, T. Okuda, X. Wang, S. Takeda, and H. Kuroda, "Inter-radar interference analysis and concept of scalable fast chirp FMCW radar for automotive applications," in *Proc. 20th Int. Radar Symp.*, 2019, pp. 1–8.

[13] F. Roos, J. Bechter, C. Knill, B. Schweizer, and C. Waldschmidt, "Radar sensors for autonomous driving: Modulation schemes and interference mitigation," *IEEE Microw. Mag.*, vol. 20, no. 9, pp. 58–72, Sep. 2019.

[14] S. Alland, W. Stark, M. Ali, and M. Hegde, "Interference in automotive radar systems: Characteristics, mitigation techniques, and current and future research," *IEEE Signal Process. Mag.*, vol. 36, no. 5, pp. 45–59, Sep. 2019.

[15] A. Bourdoux, U. Ahmad, D. Guermandi, S. Brebels, A. Dewilde, and W. Van Thillo, "PMCW waveform and MIMO technique for a 79 GHz CMOS automotive radar," in *Proc. IEEE Radar Conf.*, 2016, pp. 1–5.

[16] Z. Xu and Q. Shi, "Interference mitigation for automotive radar using orthogonal noise waveforms," *IEEE Geosci. Remote Sens. Lett.*, vol. 15, no. 1, pp. 137–141, Jan. 2018.

[17] A. Bourdoux and M. Bauduin, "PMCW waveform cross-correlation characterization and interference mitigation," in *Proc. 17th Eur. Radar Conf.*, 2021, pp. 164–167.
[18] J. Reneau and R. R. Adhami, "Phase-coded LFMCW waveform analysis for short range measurement applications," in *Proc. IEEE Aerosp. Conf.*, 2014, pp. 1–6.
[19] S. D. Blunt, M. Cook, J. Jakabosky, J. De Graaf, and E. Perrins, "Polyphase-coded FM (PCFM) radar waveforms, Part I: Implementation," *IEEE Trans. Aerosp. Electron. Syst.*, vol. 50, no. 3, pp. 2218–2229, Jul. 2014.
[20] P. M. McCormick, C. Sahin, S. D. Blunt, and J. G. Metcalf, "FMCW implementation of phase-attached radar-communications (PARC)," in *Proc. IEEE Radar Conf.*, 2019, pp. 1–6.
[21] F. Uysal, "Phase-coded FMCW automotive radar: System design and interference mitigation," *IEEE Trans. Veh. Technol.*, vol. 69, no. 1, pp. 270–281, Jan. 2020.
[22] F. Lampel, R. F. Tigrek, A. Alvarado, and F. M. J. Willems, "A performance enhancement technique for a joint FMCW radcom system," in *Proc. 16th Eur. Radar Conf.*, 2019, pp. 169–172.
[23] F. Lampel et al., "System level synchronization of phase-coded FMCW automotive radars for radcom," in *Proc. 14th Eur. Conf. Antennas Propag.*, 2020, pp. 1–5.
[24] U. Kumbul, N. Petrov, F. van der Zwan, C. S. Vaucher, and A. Yarovoy, "Experimental investigation of phase coded fmcw for sensing and communications," in *Proc. 15th Eur. Conf. Antennas Propag.*, 2021, pp. 1–5.
[25] U. Kumbul, F. Uysal, C. S. Vaucher, and A. Yarovoy, "Automotive radar interference study for different radar waveform types," *IET Radar, Sonar Navigation*, vol. 16, no. 3, pp. 564–577, 2022. [Online]. Available: https://ietresearch.onlinelibrary.wiley.com/doi/abs/10.1049/rsn2.12203
[26] R. J. Doviak and D. S. Zrnić, *Doppler Radar and Weather Observations*. New York, NY, USA: Academic Press, 1993.
[27] T. J. Rouphael, *RF and Digital Signal Processing for Software-Defined Radio: A. Multi-Standard Multi-Mode Approach*. Amsterdam, The Netherlands: Newnes, 2009.
[28] M. K. Simon, *Bandwidth-Efficient Digital Modulation With Application to Deep Space Communications*. Hoboken, NJ, USA: Wiley, 2003.
[29] T. Svedek, M. Herceg, and T. Matić, "A simple signal shaper for GMSK/GFSK and MSK modulator based on sigma-delta look-up table," *Radioengineering*, vol. 18, pp. 230–237, 2009.
[30] A. Papoulis, *Systems and Transforms With Applications in Optics*. New York, NY, USA: McGraw-Hill, 1968.
[31] O. A. Krasnov, L. P. Ligthart, Z. Li, P. Lys, and F. van der Zwan, "The PARSAX - full polarimetric FMCW radar with dual-orthogonal signals," in *Proc. Eur. Radar Conf.*, 2008, pp. 84–87.

Utku Kumbul (Graduate Student Member, IEEE) received the B.Sc. (Hons.) degree in electrical and electronics engineering (main major) and the second B.Sc. (Hons.) degree in computer engineering (double major) from the Department of Electrical and Electronics Engineering and the Department of Computer Engineering (Double Major Program), Atilim University, Ankara, Turkey, in 2014 and 2015, respectively, and the M.Sc. degree in electrical and electronics engineering from the TOBB University of Economics and Technology, Ankara, Turkey, in 2017. He is currently working toward the Ph.D. degree in electrical engineering from the Delft University of Technology, Delft, The Netherlands.

Between 2017 and 2018, he was a Hardware Engineer with Havelsan Ehsim, Air Electronic Warfare Systems Engineering, Inc., Ankara, Turkey, where he was part of the passive radar and decoy projects. His current research interests include waveform design, radar signal processing, interference mitigation, MIMO systems, and automotive radars.

He is a Reviewer of *IEEE Transactions on Aerospace and Electronic Systems* and *IET Radar, Sonar and Navigation*.

Nikita Petrov received the Engineering degree in radio-electronic control systems from Baltic State Technical University "VOENMEH" D.F. Ustinov, Saint Petersburg, Russia, in 2012, and the Ph.D. degree in radar signal processing from the Delft University of Technology, Delft, The Netherlands, in 2019.

Since then, he has been a Postdoctoral Researcher with the Microwave Sensing, Signals and Systems Section, Faculty of Electrical Engineering, Mathematics, and Computer Science, Delft University of Technology. Since 2022, he has been with NXP Semiconductors, Eindhoven, The Netherlands. His research interests include modern radar technologies, radar signal processing, multichannel and multiband signals and systems, and high resolution and automotive radars.

He is currently a Reviewer of the IEEE TRANSACTIONS ON AEROSPACE AND ELECTRONIC SYSTEMS and the IEEE TRANSACTIONS ON GEOSCIENCE AND REMOTE SENSING.

Cicero S. Vaucher (Senior Member, IEEE) received the Ph.D. degree in electrical engineering from the University of Twente, Enschede, The Netherlands, in 2001.

From 1990 to 2006, he was with Philips Research Laboratories, Eindhoven, The Netherlands,, and then he joined NXP Semiconductors. He is currently an Automotive Radar Product Architect with the ADAS Product Line. He is also a part-time Professor with TU Delft, Delft, The Netherlands, where he is working on mmWave front-ends. He is the author of *Architectures for RF Frequency Synthesizers* (Kluwer, 2002), coauthor of *Circuit Design for RF Transceivers* (Kluwer, 2001), and (co-)inventor of 28 unique patent families. His research interests include microwave and mm-Wave transceiver architectures, radar system implementation and signal processing, and implementation of circuit building blocks.

Dr. Vaucher was a member of the Technical Programme Committee of the IEEE Custom Integrated Circuits Conference (CICC) from 2005 to 2013, acting in the wireless subcommittee. He is on the IEEE-MTT Connected and Autonomous Systems Technical Committee 27. He is an NXP Technical Fellow.

Alexander Yarovoy (Fellow Member, IEEE) received the Diploma (Hons.) in radiophysics and electronics from the Kharkov State University, Kharkiv, Ukraine, in 1984, and the Candidate of Physics and Mathematics Scientific and Doctor Physics and Mathematics Scientific degrees in radiophysics in 1987 and 1994, respectively.

In 1987, he joined the Department of Radiophysics, Kharkov State University, as a Researcher and became a Full Professor there in 1997. From September 1994 to 1996, he was a Visiting Researcher with the Technical University of Ilmenau, Ilmenau, Germany. Since 1999, he has been with the Delft University of Technology, Delft, The Netherlands. Since 2009, he has been a Chair of Microwave Sensing, Systems and Signals. He has authored or coauthored more than 500 scientific or technical papers, seven patents, and 14 book chapters. His main research interests include high-resolution radar, microwave imaging, and applied electromagnetics (in particular, UWB antennas).

Dr. Yarovoy was the recipient of the European Microwave Week Radar Award for the paper that best advances the state-of-the-art in radar technology in 2001 (together with L.P. Ligthart and P. van Genderen) and in 2012 (together with T. Savelyev), and Best Paper Award of the Applied Computational Electromagnetic Society in 2010 (together with D. Caratelli). He was the General TPC Chair of the 2020 European Microwave Week, as the Chair and TPC Chair of the Fifth European Radar Conference, as well as the Secretary of the First European Radar Conference. He was also the Co-Chair and TPC Chair of the Tenth International Conference on GPR. From 2011 to 2018, he was an Associate Editor for the *International Journal of Microwave and Wireless Technologies,* and a Guest Editor of five special issues of the IEEE transactions and other journals. From 2008 to 2017, he was the Director of the European Microwave Association.